Università degli Studi di Padova

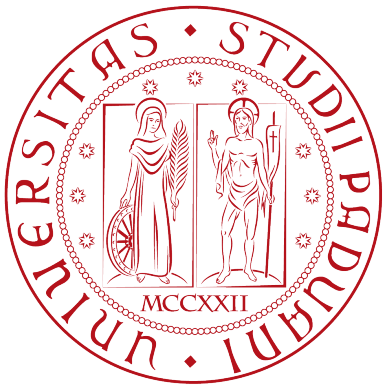

Dipartimento di Fisica e Astronomia "Galileo Galilei"

Laurea Magistrale in Fisica

The Search of Axions Through Polarized Matter

Laureando:
Nicolò Crescini
1104948

Relatore:
Prof. Giovanni Carugno
Controrelatore:
Prof. Jean-Pierre Zendri

Anno Accademico 2015/2016

"Not all those who wander are lost."
J.R.R. Tolkien

Alla mia famiglia.

Abstract

The QCD axion is an hypothetical particle introduced to solve the strong CP problem of standard model of particle physics and are of interest as a possible component of cold dark matter. The allowed couplings between particles is determined by the vertices of the spin-0 bosons: the pseudoscalar interaction is always spin-dependent, while, in the non-relativistic limit, the scalar interaction can be treated as spin-independent. Thus, in a multipole expansion, the two fields are described by the "dipole" (pseudo-scalar coupling g_p) and "monopole" (scalar coupling g_s) moments, respectively.
Aim of the experiment is to improve the measured limits for the $g_p g_s$ product, for different values of the axion mass, this interaction arises between a nucleus N and the spin of an electron e^-.

Even if the coupling between single particles is weak, a macroscopic sample with the order of 10^{23} atoms, could produce a light coherent bosonic field that can be measured. In the axion scenario, J.E. Moody and F. Wilczek showed that a new macroscopic force, mediated by the exchange of axions, acts on electron spins, and that such force can be described in terms of the potential of a field. The effective field interacts with electron spins of matter, can be associated to an effective magnetic field and detected by measuring the induced changes of magnetization. The purpose of the experiment is to detect with a SQUID a magnetization signal which is not produced by a magnetic field but by a material with high nuclei density.

The source consists of large unpolarized masses that provides the monopole part of the interaction g_s^N while the dipole part g_p^e depends on the electron spins of the crystal. The interaction causes a change in the magnetization of the sample and induces a change of the magnetic flux collected by a coil surrounding the crystal. As the interaction potential is generated by pseudoscalar exchange rather than by vector gauge boson exchange, this field does not satisfy the Maxwell's equations, therefore it is possible to shield the apparatus from electromagnetic noise sources without affecting the signal. A rotating wheel with evenly spaced lead disks allows for a source mass with a variable distance, while a cryostat houses the detector in lHe, placed as close as possible to the moving source; this allows a periodic modulation of the signal. To further increase the sensitivity of the apparatus, the signal is amplified with a resonant RLC circuit, tuned at the signal frequency given by the rotating wheel. This circuit will be coupled with the pick-up of the SQUID and the resulting signal will be increased by its Q-factor.

The main efforts to measure this interaction has been performed by Ni *et al.* and Adelberger *et al.*, this experiment lowered this limits of one

orders of magnitude. Considering an integration time of 4 h, the minimum detected signal is $B_{\rm eff,min} \simeq 10^{-17}$ T, with a resultant limit on the coupling $g_p^e g_s^N/\hbar c \lesssim 10^{-30}$. Using a resonant pick-up with $Q \simeq 10^4$ the limit becomes $B_{\rm eff,min} \simeq 10^{-22}$ T, therefore the limit on the coupling is $g_p^e g_s^N/\hbar c \lesssim 10^{-34}$.

Abstract

L'assione di QCD è una particella introdotta per risolvere il problema della CP forte del modello standard della fisica delle particelle ed è di interesse come candidato componente di materia oscura fredda. Gli accoppiamenti permessi sono determinati dai vertici di un bosone a spin nullo: l'interazione pseudoscalare dipende sempre dallo spin, mentre, nel limite non relativistico, l'interazione scalare viene considerata indipendente dallo spin. Quindi, in un'espansione multipolare, i due campi sono descritti come "dipolo" (accoppiamento pseudoscalare g_p) e "monopolo" (accoppiamento scalare g_s). L'obiettivo dell'esperimento è migliorare gli attuali limiti misurati per l'intensità dell'accoppiamento $g_p^e g_s^N$, per diversi valori della massa dell'assione, quest'interazione avviene tra un nucleone N e lo spin di un elettrone e^-.

Anche se l'accoppiamento di singola particella è molto debole, un campione macroscopico composto da circa 10^{23} atomi, può produrre un leggero campo bosonico coerente che può essere misurato. Nell'ambito della fisica degli assioni, J.E. Moody and F. Wilczek hanno mostrato che una nuova forza macroscopica, mediata dallo scambio di assioni, agisce sullo spin elettronico, e ne hanno descritto il potenziale. Tale campo, che interagisce con lo spin degli elettroni della materia, può essere descritto in termini di un campo magnetico efficace e rivelato misurando un cambiamento di magnetizzazione indotto. Il principio alla base dell'esperimento, è la rivelazione tramite SQUID di un cambiamento di magnetizzazione anomalo, prodotto non da un campo magnetico, ma da un materiale ad alta densità di nuclei.

Le sorgenti del segnale sono grandi masse non polarizzate che costituiscono la parte monopolare g_s^N dell'interazione, mentre la parte dipolare g_p^e è costituita dagli spin elettronici di un cristallo. L'interazione crea quindi un cambio di magnetizzazione del campione e induce quindi una variazione del flusso magnetico collezionato dalla bobina che circonda il cristallo. Dal momento che il potenziale dell'interazione è generato da mediatori pseudoscalari invece che da bosoni vettori di gauge, il campo generato non soddisfa le equazioni di Maxwell, ed è quindi possibile schermare l'apparato dalle sorgenti di rumore elettromagnetico senza compromettere il segnale. Un disco rotante con blocchi di piombo o rame equispaziati permette alle masse sorgente di avere distanza variabile dal rivelatore, che è posizionato in un criostato ad elio liquido più vicino possibile alle sorgenti in movimento; questo permette di modulare il segnale. Per incrementare ulteriormente la sensibilità dell'apparato, il segnale viene amplificato con un circuito RLC risonante, costruito in modo che la frequenza di risonanza coincida con quella

del segnale dato dalle masse rotanti. Il circuito sarà quindi accoppiato con il pick-up dello SQUID e il segnale risultante verrà incrementato in base al fattore di qualità Q del circuito.

I più recenti tentativi di misurare tale interazione sono stati fatti da Ni *et al.* e Adelberger *et al.*, questo esperimento ha abbassato tali limiti di un ordine di grandezza. Utilizzando un tempo di integrazione di 4 ore, il campo minimo misurato è $B_{\text{eff}} \simeq 10^{-17}\,\text{T}$, con un conseguente limite sull'accoppiamento $g_p^e g_s^N/\hbar c \lesssim 10^{-30}$. Utilizzando il pick-up risonante con un $Q \simeq 10^4$ il limite diventa $B_{\text{eff,min}} \simeq 10^{-22}\,\text{T}$, e il limite sull'accoppiamento diviene $g_p^e g_s^N/\hbar c \lesssim 10^{-34}$.

Contents

Chapter 1

Theoretical introduction

In particle physics, a spontaneously broken symmetry implies the existence of a Nambu-Goldstone boson [1]. If the symmetry is exact, the resulting boson is always massless, and couples with fermions with a coupling constant of $g_p = m_f/F$, where m_f is the mass of the fermion and F is the energy scale of the spontaneously broken symmetry. On the other hand, massive bosons are produced by symmetries which are not exact, like QCD pions for the chiral symmetry, and their mass is $m_b = \Lambda^2/F$ (where Λ is the explicit symmetry-breaking scale of the effective Lagrangian).
The search of broken symmetries at extremely high energies can be performed through the search of such exotic pseudo-Goldstone bosons, which mediates long-range ultraweak forces. The detection of a new force will account for the presence of a boson and, therefore, of a broken symmetry; the axion is a pseudo-Goldstone boson arising from the breaking of the Peccei-Quinn symmetry [2] and it could mediate forces which are dependent on its coupling.

1.1 Axions in the framework of the SM

In the 1970's the strong interactions had a puzzling problem, which became particularly clear with the development of QCD. The QCD Lagrangian for N flavors in the limit of vanishing quark masses $m_f \to 0$ has a large global vector-axial (V-A) symmetry: $U(N)_V \times U(N)_A$. Since $m_u, m_d << \Lambda_{\rm QCD} \simeq 200\,\text{MeV}$, it is known that, at least for these quarks, the limit of sending the quark masses to zero is sensible. Thus one would expect the strong interactions to be approximately $U(2)_V \times U(2)_A$ [3]. What one finds experimentally is that, indeed, the vector symmetry corresponding to isospin times baryon

number $U(2)_V = SU(2)_I \times U(1)_B$ is a good approximate symmetry of nature, as manifested by the appearance of nucleon and pion multiplets in the spectrum of hadrons. Although pions are light, there are no signs of another light state in the hadronic spectrum, since $m_\eta^2 \gg m_\pi^2$.
After Weinberg's suggestion [4] that there was not a $U(1)_A$ symmetry in strong interactions, t'Hooft [5, 6] realized that the QCD has a more complicated vacuum structure than expected. The $U(1)_A$ symmetry is in fact only an apparent symmetry of the QCD Lagrangian, in the limit of vanishing quark masses. However, associated with this more complicated QCD vacuum there is a phase parameter θ and only if this parameter is very small CP is not very badly broken in the strong interactions. So the solution of the $U(1)_A$ problem begets a different problem, the absence of CP violation in the strong interactions.
The vacuum state is a superposition of n-vacua and it is called the θ-vacuum:

$$|\theta\rangle = \sum_n e^{-in\theta} |n\rangle \,. \tag{1.1}$$

Calculating the vacuum to vacuum transition amplitude one obtains

$$\langle \theta_+ | \theta_- \rangle = \sum_{n,m} e^{-in\theta} e^{im\theta} \langle m|n\rangle = \sum_\nu e^{i\nu\theta} \sum_n \langle (n+\nu)_+ | n_- \rangle \,, \tag{1.2}$$

the difference in winding numbers ν is

$$\nu = \frac{g^2}{32\pi^2} \int d^4x F_i^{\mu\nu} \tilde{F}^i_{\mu\nu}, \tag{1.3}$$

where $\tilde{F}^a_{\mu\nu} = \frac{1}{2}\epsilon_{\mu\nu\varrho\sigma} F^{a\varrho\sigma}$. Using the usual path integral representation for the vacuum to vacuum amplitude $\langle \theta_+ | \theta_- \rangle$ one sees that the solution of the $U(1)_A$ problem actually adds an extra term to the QCD Lagrangian

$$\mathcal{L}_\theta = \frac{\theta g^2}{32\pi^2} F_i^{\mu\nu} \tilde{F}^i_{\mu\nu} \tag{1.4}$$

which violates parity and time reversal invariances, but conserves charge conjugation invariance, so it violates CP. Naturally the value of this parameter is expected to be of the order of the unity, and is to be experimentally determined. The effective physical CP-violating parameter in the Standard Model is $\bar{\theta}$, the phase angle including both the strong and weak interactions $\bar{\theta} = \theta + \arg(\det M)$ (where M is the quark mass matrix). It has to be noticed that the term in Eq.(1.4) is a permitted term of the Standard Model lagrangian, in fact it respects the symmetries of the model and is

renormalizable, indeed $[\mathcal{L}_\theta] = [\mathrm{M}]^4$. It is often omitted because of the smallness of the θ parameter, nevertheless it violates the charge conjugation and parity symmetries. Experimentally this violation would be expressed in an anomalous neutron electric dipole moment d_n,

$$|d_n| = \frac{e}{m_n}\Big(\frac{m_q}{m_n}\Big)|\bar{\theta}|, \tag{1.5}$$

where m_n (m_q) is the neutron (a light quark) mass, e is the unit of electric charge. A strong experimental bound of $d_n \lesssim 3 \times 10^{-26}\,\mathrm{e\,cm}$ [7] suggests that the angle $\bar{\theta}$ should be very small, $\bar{\theta} \lesssim 10^{-10}$ [8–10]. Despite θ can take any value, a value very small or zero lead to a "naturalness problem", as it is expected to be $O(1)$. In fact a Universe where CP is violated strongly seems as viable as one where it is not.

Introducing an additional chiral symmetry is a very natural solution for this problem since this chiral symmetry, effectively, rotates the θ-vacua away, leading to a dynamical interpretation of the angle. This symmetry, introduced by Peccei and Quinn [2] and therefore known as $U(1)_{\mathrm{PQ}}$, is necessarily spontaneously broken at high energies, and its introduction into the theory effectively replaces the static CP-violating angle with a dynamical CP-conserving field, the axion $a(x)$. This particle is the Nambu-Goldstone boson of the broken PQ symmetry, which, as a result of the $U(1)_{\mathrm{PQ}}$ transformation translates

$$a(x) \xrightarrow{U(1)_{\mathrm{PQ}}} a(x) + \alpha f_a, \tag{1.6}$$

where f_a is the energy associated with the spontaneously broken symmetry, such that $\theta = a(x)/f_a$. Formally, the axionic interaction must be added to the Standard Model Lagrangian ($\mathcal{L}_{\mathrm{SM}}$) to make it PQ-invariant

$$\mathcal{L} = \mathcal{L}_{\mathrm{SM}} + \frac{\bar{\theta} g^2}{32\pi^2} F_i^{\mu\nu}\tilde{F}^i_{\mu\nu} - \frac{1}{2}(\partial_\mu a)(\partial^\mu a) + \mathcal{L}_{int}[\partial_\mu a;\psi] + \xi\frac{a}{f_a}\frac{g^2}{32\pi^2}F_i^{\mu\nu}\tilde{F}^i_{\mu\nu}. \tag{1.7}$$

In Eq.(1.7) the last term is needed to ensure that the $U(1)_{\mathrm{PQ}}$ current has indeed a chiral anomaly

$$\partial_\mu j^\mu_{\mathrm{PQ}} = \xi\frac{g^2}{32\pi^2}F_i^{\mu\nu}\tilde{F}^i_{\mu\nu}. \tag{1.8}$$

This term also represents an effective potential for the axion field, with the minimum in $< a >= -f_a\bar{\theta}/\xi$ and , as an effective potential, it is not renormalizable. Since at the minimun the $\bar{\theta}$-term is cancelled out, this provides a dynamical solution to the strong CP problem. An expansion of

the potential around the minimum gives the axion a mass [11]. In the Peccei Quinn model [2], the symmetry breakdown coincided with that of electroweak breaking $f_a = v_F \simeq 250\,\mathrm{GeV}$, however, this is not necessary. The original PQ model, was long ago ruled out by experiment, but the so called "invisible axion" model, where $f_a \gg v_F$, are still viable [12]. This models introduce axions which carry PQ charge but are singlets of $SU(2)_L \times U(1)_Y$. The first model, due to Kim [13] and Shifman, Vainshtein and Zakharov [14] (the so-called KSVZ Model), introduces a scalar field σ with $f_a =< \sigma >\gg v_F$ and a superheavy quark Q with $M_Q \simeq f_a$ as the only fields carrying PQ charge. The second one, due to Dine, Fischler and Srednicki and Zhitnisky [15] (called DFSZ Model), adds to the PQ model a scalar field ϕ which carry PQ charge and such that $f_a =< \phi >\gg v_F$. Although the KSVZ and DFSZ axions are very light, very weakly coupled and very long-lived, they are not totally invisible.

1.1.1 Astrophysical and cosmological bounds

As the axion is not involved in the standard model and in other astrophysical and cosmological theories, its mass have to be small (or large) enough not to affect them critically. The first astrophysical bound is given by the stellar energy loss, since low mass weakly-interacting particles (like neutrinos and possibly axions or gravitons) are produced in astrophysical plasma and transport energy out of stars [16]. The observed stellar lifetimes give rise to bounds on the coupling of these particles to matter and radiation, in fact processes such as the Primakoff effect ($\gamma\gamma \to a$) and compton production ($\gamma e \to ae$) would produce losses in the stellar luminosity. Since e.g. solar luminosity is fixed, this losses lead to an enhanced nuclear energy production and therefore to enhanced neutrino fluxes, measured, for example, by the SNO experiment. Similar limits are given by the variation of the cooling period in White Dwarfs, the measured period decrease of star G117-B15A led to a limit of $f_a \gtrsim 7 \times 10^8\,\mathrm{GeV}$. The energy loss is inversely proportional to f_a^2, and hence proportional to m_a^2 thus axions must be light enough, so as not to affect stellar evolution. Another bound on m_a come from SN1987a, since axion emission through the process $NN \to NNa$ in the core collapse affects the neutrino spectrum [17]. Typical bounds obtained from astrophysics require axions to be lighter than $m_a < 1 - 10^{-3}\,\mathrm{eV}$ [18].

Cosmology gives an upper bound to f_a and a lower bound to m_a [15,19–21]. Applying the PQ phase transition to the Universe, at a temperature $T \simeq f_a$ the QCD anomaly is not effective, sice $f_a \gg \Lambda_{\mathrm{QCD}}$. Eventually, when the Universe cools down and $T \simeq \Lambda_{\mathrm{QCD}}$ the axion obtains mass, not

instantaneously but fluctuating. This axion oscillations contribute to the Universe energy density and axions act as cold dark matter. The energy of oscillations is proportional to f_a and thus bounds the energy density of cold dark matter, providing an upper bound of f_a and therefore a lower bound to m_a.
A calculation by Fox, Pierce and Thomas [22] provide the contribution to the Universe's energy density due to axions:

$$\Omega_a h^2 = 0.5\Big(\frac{f_a/\xi}{10^{12}\,GeV}\Big)^{7/6}(\theta_i^2 + (\sigma_\theta)^2)\gamma, \tag{1.9}$$

where ξ is the coefficient of the PQ anomaly ($\xi = 1$ in the way was defined f_a, for both DFSZ and KSVZ models), θ_i is the misalignment value for $< a > /f_a$, σ_θ is its mean squared fluctuation and γ is a possible dilution factor for the energy density produced by axion oscillations.
Using the WMAP bound on cold dark matter [23]

$$\Omega_a h^2 < 0.12, \tag{1.10}$$

assuming no dilution (i.e. $\gamma = 1$), using an average $\theta_i^2 \simeq \pi^2/3$ and neglecting the fluctuations, the data gives the following cosmological bound for the PQ scale

$$f_a < 10^{12}\,\mathrm{GeV} \quad \text{or} \quad m_a > 2.1 \times 10^{-5}\,\mathrm{eV}. \tag{1.11}$$

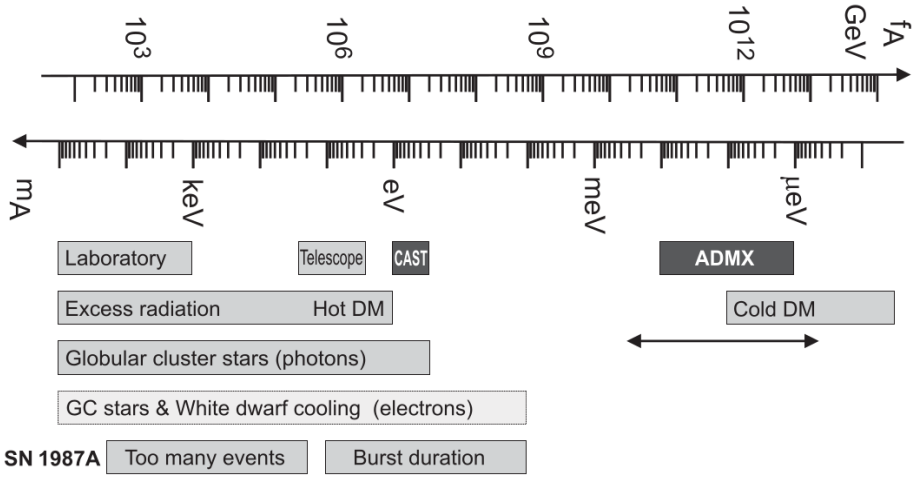

Figure 1.1: Summary of cosmological and astrophysical constraints for axions [24]. See text for details.

Moreover, in the plot in Fig.(1.1) the areas marked "ADMX" and "CAST" show the near future search ranges.

1.2 Axionic interactions

Axions can be detected through the macroscopic forces which they mediate, the possible forces are determined by the allowed couplings that are the vertices of the spin-0 bosons [25]. There are only two possibilities for coupling with fundamental fermions, the scalar and pseudoscalar vertex, that can be analyzed in the momentum space using the Gordon decomposition. For pure spacelike momentum transfer $\boldsymbol{q}$, they become, for the scalar

$$g_s a(q)\bar{\psi}(p_f)\psi(p_i) = g_s a(q)\Big(\frac{p_\mu p^\mu}{M^2}\bar{\psi}(p_f)\psi(p_i) - i\frac{p_\mu q_\nu}{2M^2}\bar{\psi}(p_f)\sigma^{\mu\nu}\psi(p_i)\Big), \tag{1.12}$$

and pseudoscalar,

$$\begin{aligned} g_p a(q)\bar{\psi}(p_f)i\gamma_5\psi(p_i) &= g_p a(q)\frac{q^\mu}{2M}\bar{\psi}(p_f)i\gamma_5\gamma_\mu\psi(p_i) \\ &= g_p a(q)\frac{\boldsymbol{q}}{2M}\psi^+(p_f)i\boldsymbol{\Sigma}\psi(p_i); \end{aligned} \tag{1.13}$$

where $p_f = p + q/2$ and $p_i = p - q/2$ are the final and initial on-shell momenta, M is the fermion mass and $\boldsymbol{\Sigma}$ is the diagonal spin matrix.
The pseudoscalar interaction is always spin-dependent, while, in the non-relativistic limit, the scalar interaction can be treated as spin-independent (see Fig.(1.2)). Thus, in a multipole expansion, the two fields are described by the "dipole" (pseudo-scalar coupling g_p) and "monopole" (scalar coupling g_s) moments, respectively. Calling the vertices G_s, p for scalar and pseudoscalar respectively, the two-fermion potential can be calculated with the inverse Born approximation as

$$V(r) = \int \frac{d^3q}{(2\pi)^3}\frac{G_v G_w e^{i\boldsymbol{q}\cdot\boldsymbol{r}}}{\boldsymbol{q}^2 + m_a^2}; \qquad v, w = p, s. \tag{1.14}$$

The potential in Eq.(1.14) can lead to three different combination, this allow the existence of the same number of distinct forces.

Since the aim of the experiment is to the detect the *monopole-dipole* coupling, only that will be analyzed in this Section, however a brief discussion of the other two couplings is performed in Appendix A.
Fig.(1.2) reports the Feynman diagram of the $g_p g_s$ interaction, where the

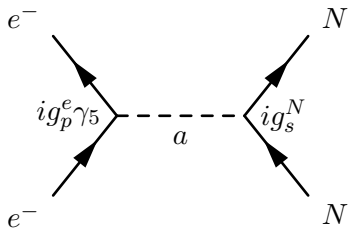

Figure 1.2: Interaction diagram of a scalar-pseudoscalar coupling between a nucleus N and an electron e^-. N is unpolarized and interacts at the scalar vertex with the coupling constant g_s^N, whereas e^- is polarized and interacts at the pseudoscalar vertex with the coupling constant g_p^e. The mediator is the axion a and the interaction strength is proportional to $g_s^N g_p^e$.

considered fermions are an electron e^- and a nucleus N; the superscripts on the coupling constants are named after these. The single particle *monopole-dipole* coupling (e.g. of electronic spin with nuclei) can be derived from Eq.(1.14), using a scalar and a pseudoscalar vertex (e.g. $v = s$ and $w = p$). The calculation yields

$$V_{md}(\boldsymbol{r}) = \frac{\hbar g_p^e g_s^N}{8\pi m_e c}\Big[(\hat{\boldsymbol{\sigma}}\cdot\hat{\boldsymbol{r}})\Big(\frac{1}{r\lambda_a}+\frac{1}{r^2}\Big)\Big]e^{-\frac{r}{\lambda_a}}, \tag{1.15}$$

where λ_a is the Compton wavelength of the axion, g_p^e and g_s^N are the coupling constants of the Yukawa interaction, c is the speed of light in vacuum, m_e is the mass of the electron, $\hat{\boldsymbol{\sigma}}$ is the vector of Pauli spin matrices, and r and $\hat{\boldsymbol{r}}$ are the distance and unit vector between the monopole and the dipole, respectively [1, 25, 26]. This potential describes the interaction between two single particles and the axion Compton wavelength determines the range of the interaction. Since $\lambda_a = h/m_a c$ is macroscopic, a long-range force is produced.

Thanks to the presence of the Pauli matrices vector term, this interaction can be written in the form of an effective magnetic field. The amplitude of this field can be estimated using the formula of the potential energy of an electron in an external magnetic field $\mathbf{B}$

$$U = \mu_e \hat{\boldsymbol{\sigma}}\cdot\boldsymbol{B}, \tag{1.16}$$

where $\mu_e = e\hbar/2m_e$ is the Bohr's magneton and $\mu_e\boldsymbol{\sigma}$ is the spin magnetic moment of an electron. By recasting Eq.(1.15) as Eq.(1.16) one gets the explicit expression of this field

$$\boldsymbol{B}_{\text{eff},md}(\boldsymbol{r}) = -\frac{g_p^e g_s^N}{4\pi e c}\hat{\mathbf{r}}\Big(\frac{1}{r\lambda_a}+\frac{1}{r^2}\Big)e^{-\frac{r}{\lambda_a}}. \tag{1.17}$$

Even if the coupling between single particles is weak, a macroscopic sample, with the order of 10^{23} atoms, could produce a light coherent bosonic field that can be measured. From the integration of this equation over the volume of the source, it is possible calculate the amplitude of the equivalent measurable field. However, this field is not an ordinary magnetic field, since it couples to the spin of the fermion, and is independent of fermion magnetic moment, electric charges, moving charges and angular momentum. As the interaction potential is generated by pseudoscalar exchange rather than by vector gauge boson exchange, this field does not satisfy the Maxwell's equations.

1.2.1 Couplings magnitude

The different axion models ([13,14,27]) do not provide a unique value for the coupling constants g_p and g_s. The axion mass is determined by the values of f_a, the energy scale at which the Peccei-Quinn symmetry is broken. In addiction, the presence of an axion vacuum angle expectation $\theta \neq 0$ allows for monopole-dipole coupling. The values of the couplings as a function of the mass of the axion m_a reads

$$g_p g_s = \frac{\theta\sigma}{f_a^2} \frac{m_u m_d}{(m_u + m_d)^2} m_a, \tag{1.18}$$

where m_u and m_d are the masses of the up and down quarks [25]. The angle θ in the conservative Kobayashi-Maskawa model, is expected in the 10^{-14} range and the pion-nucleon σ term is taken to be 60 MeV [28]. This σ term takes into account the strange quark component of the pion, it is often used in the chiral perturbation theory, which aim is to give a description of QCD at low energies[1]. The dimensionless axion coupling strengths for the three interaction types (Eq.(1.18), (A.2), (A.5)) are reported in Fig.(1.3) to better understand their magnitude. It is worth noticing that this value of θ is a limit from below, and that other models suggest much higher values, up to $\theta \simeq 10^{-10}$, increasing the monopole-dipole coupling of several orders of magnitude.

As briefly discussed, cosmological and astrophysical considerations suggest a preferred value of $f_a \simeq 10^{12}$ GeV [15, 19–21]; in this case axions would account for the missing mass of the universe. Moreover, f_a must be $< 10^{13}$ GeV, otherwise axion would overdominate the evolution of the Universe (overclosure problem). The values of θ, σ and f_a set the axion window

[1] Note that QCD is perturbative only at high energies.

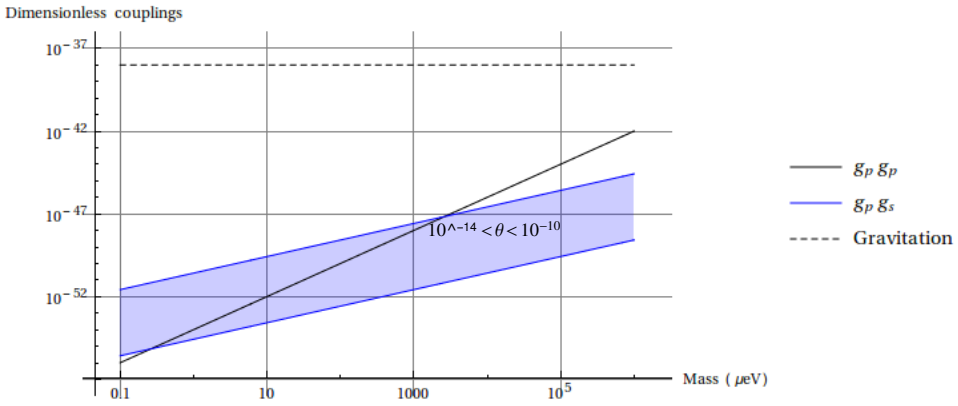

Figure 1.3: Dimensionless axion couplings in function of m_a and θ. The gravitational dimensionless coupling for two nucleons $\alpha_G = Gm_n^2/\hbar c$ is reported for comparison and the $g_s g_s$ term was omitted.

in the coupling-mass space [29]. The values of the other types of couplings are reported in Appendix A.

1.3 Possible experimental approaches

Since the forces mediated by spin-0 bosons are described, it is possible to attempt a measurement of this interactions. Techniques to measure very weak forces have been developed and seem suitable for the detection of axions. Axion sources are macroscopic collections of nucleons (ordinary masses) or coherent, spin-polarized electron or nucleon systems. The works to search for the spin-dependent (semi-)long-range forces, can be classified into two categories: those searching for the monopole-dipole interactions and those searching for the dipole-dipole interactions. These works are largely motivated to explore the role of spin in gravitation, and to explore the interaction associated with the exchange of a light or massless boson.

In connection with P (parity), and T (time reversal) noninvariance, Leitner and Okubo [30], and Hari Dass [31] suggested some time ago the type of spin-gravity interaction in the form given in Eq.(A.1). Fujii [32] proposed finite-range mass-mass interactions. More recently, Fischbach *et al.* [33] proposed a fifth force which violates the equivalence principle with finite-range monopole-monopole interactions and stimulated many experimental efforts. Wei-Tou Ni [6], used torsion balance with two cylindrical copper test masses and two cylindrical polarized "attracting" Dy_6Fe_23 masses to search for

finite-range mass-spin interactions with the potential of Eq.(A.1). The result showed that for the range of 3-5 cm, the upper limit of this interaction were below 1% of their gravitational interaction. Ritter *et al.* [34], in a recent experiment, used spin-polarized Dy_6Fe_{23} masses acting on unpolarized copper masses in a dynamic-mode torsion pendulum and searched for the interaction of the axion.

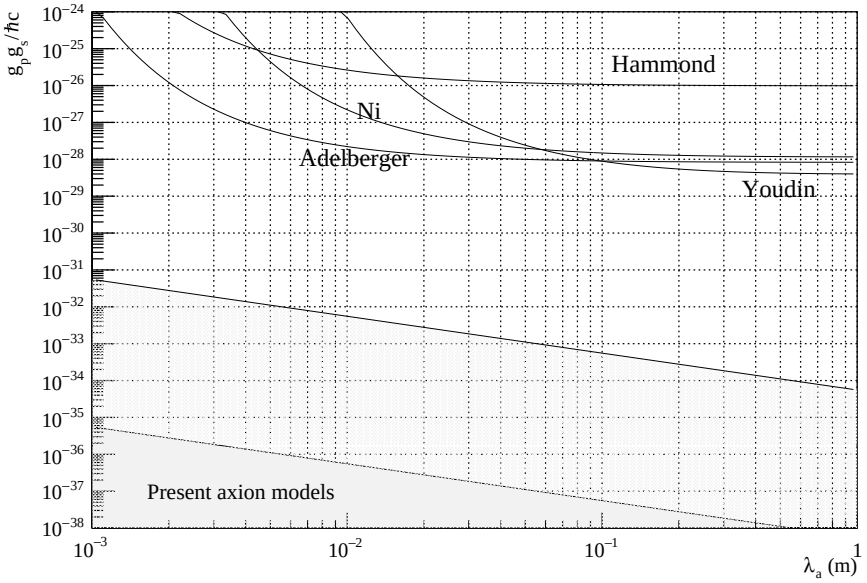

Figure 1.4: Measured limits for the $g_p g_s$ coupling compared with the axion window, for $\theta = 10^{-10}$ and $\theta = 10^{-14}$.

Vorobyov and Gitarts [35] first used induced ferromagnetism with a SQUID[2] to search for spin-dependent forces. The Cooper pairs of the superconducting shields enclosing the SQUID detecting system provide magnetic shielding. The searched-for anomalous spin interaction due to an outside body would not be shielded by these Cooper pairs. However, the ferromagnetic permeable material in their SQUID detector system was asked to be sensitive five-order beyond the actual test of these materials. To avoid this limiting factor, and to assure a clear understanding of a low-field response, this experiment have used induced paramagnetism with a

[2]A device that can be used as a very sensitive magnetometer, it will be described in Section 2.3.1.

dc-SQUID to search for spin-dependent forces. The latest and more precise measurement were reported in Fig.(1.4). In the case of Hammond and Adelberger [36,37] the measurement was performed with a torsion pendulum and rotating attractor and a new device that they refer to as the spherical superconducting torsion balance, respectively. Youdin *et al.* [38] managed compare the relative precession frequencies of Hg and Cs magnetometers as a function of the position of two lead masses with respect to an applied magnetic field. Finally, Ni *et al.* [39] performed this measurements using a paramagnetic salt TbF_3 with a dc-SQUID.

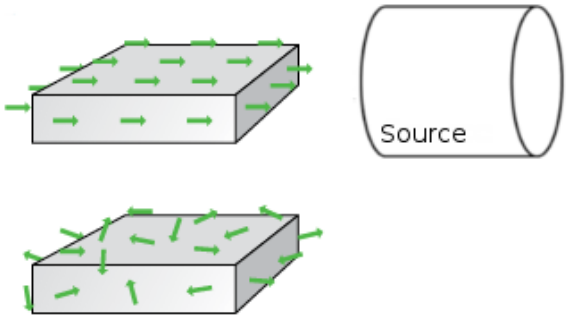

Figure 1.5: Representation of the change of magnetization due to the source.

This last approach is similar to the one of QUAX-$g_p g_s$, whose aim is to measure a force mediated by axions (or *axion-like particles*, ALPs) which has a large unpolarized mass as source and a paramagnetic crystal as a detector. The presence of the mass allows axions to mediate this spin-dependent force and change the magnetization of the sample (crystal) as represented schematically in Fig.(1.5).

This considerations hold not only for axions but also for the already mentioned ALPs. In fact the axion window is derived from a theoretical model, which still has to be confirmed. The region of space above the reported limit is already unexplored, so the absence of particles which has features similar to the one of the axion can be verified. In this sense the performed measurement, like the others reported until this point, does not test only the presence of axions, but the presence of a spin-dependent force that stands for the presence of a new particle. In fact, some of the cited authors refer to their works as generic pseudo-Goldstone bosons detector or axionlike coupling searches.
For the sake of completeness, a brief review of the present experiment testing

the coupling with photons is reported in this section. In particular, some of this works assumes that axions are the main constituents of cold dark matter, in fact cosmic observation and particle physics experiments have bracketed the unknown mass of the axion between approximately a μeV and a meV.

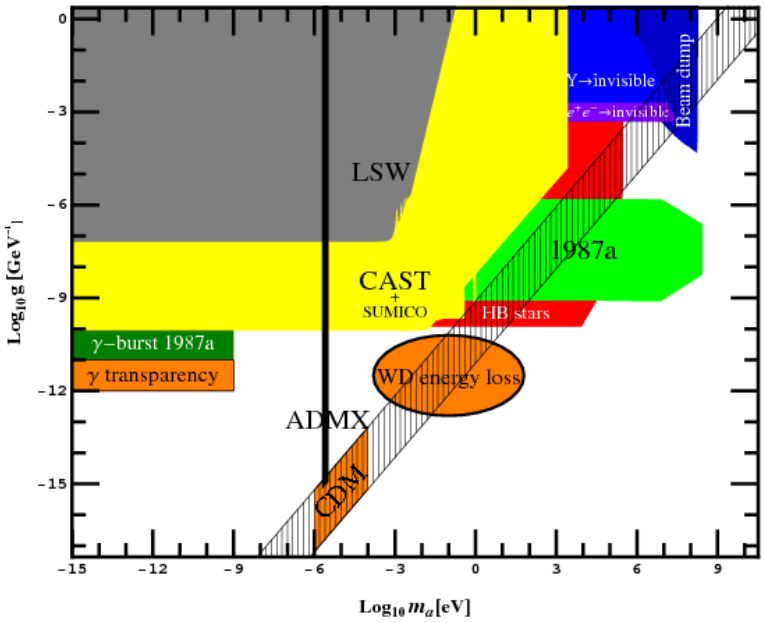

Figure 1.6: Summary of experimental constraints for axion-like-particles (two photon coupling constants vs. mass m_a of the ALP) [24], see text for details. Some astrophysical and cosmological bound are reported too.

In the plot in Fig.(1.6) the axion band is shown hatched. Here are also shown laboratory limits from photon regeneration experiments (ADMX and LSW). Note that the limit from ADMX is valid only under the assumption that the local density of ALPs at earth is given by the dark matter density. Other areas with interesting astrophysical hints are also marked in orange. It is also to be noticed that the mass region, where the axion can be the cold dark matter (the orange regions labeled "CDM" in the plots), can be extended towards smaller masses (larger $f_a \lesssim 1016\,\mathrm{GeV}$) by anthropic reasoning.

Chapter 2

Experimental Apparatus

The effective field in Eq.(1.15) interacts with electron spins of matter, and it can be detected by measuring the induced changes of matter magnetization. First efforts to measure spin-dependent forces using ferromagnets and SQUIDs are reported in Ref. [35].

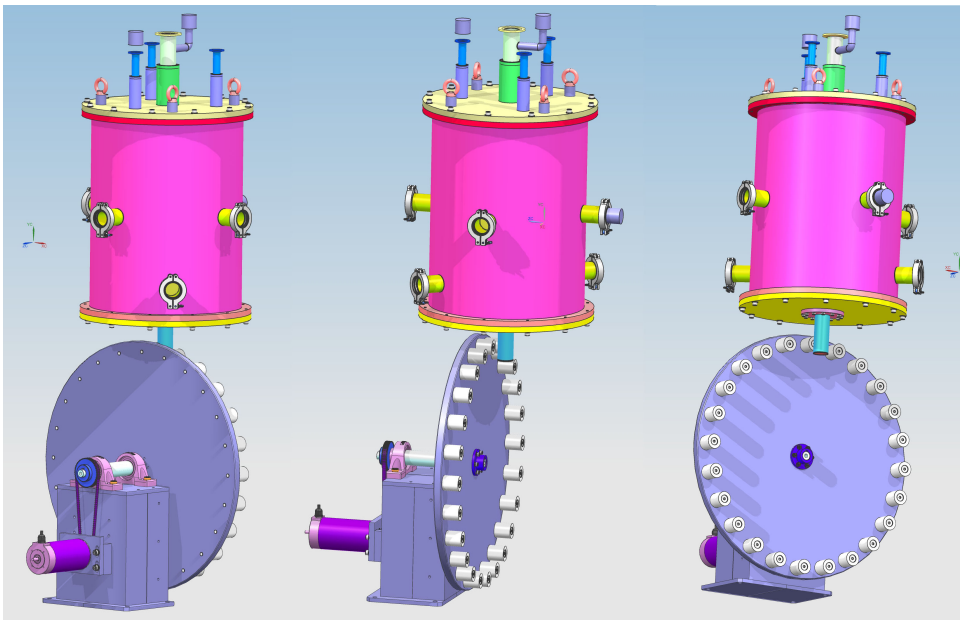

Figure 2.1: A schematic showing the QUAX-g_p-g_s apparatus for measuring the strength of $g_p g_s$ interaction. The cryostat houses the GSO crystal (detector). The rotating toothed wheel (unpolarized source) modulates in time the monopole-dipole interaction.

The approach chosen for QUAX-$g_p g_s$ (QUest for AXion) is similar, except for the substitution of the ferromagnetic sample with a paramagnetic crystal, in order to avoid domain wall noise. Aim of the experiment is to detect a magnetization signal which is not produced by a magnetic field but by a material with high nuclear density. The periodic modulation of the signal is achieved by varying the source-detector distance. Fig.(2.1) shows a schematic of the main components of the QUAX-$g_p g_s$ experiment. A rotating toothed wheel allows for a source mass with a variable distance, while a cryostat houses the detector, placed as close as possible to the moving source. Hereafter are given some details about the experimental setup, starting from the unpolarized mass sources and the paramagnetic detector, and continuing with the SQUID and readout electronics.

2.1 Source

The source consists of large unpolarized masses that provides the monopole part of the interaction. Each mass is a lead disk, 2.5 cm thick, 9.5 cm in diameter and 1.95 kg in weight. In the first experimental setup, 4 masses evenly spaced are placed on a prototype of the rotating wheel having controllable angular velocity; this allows to modulate the interaction at a given frequency.

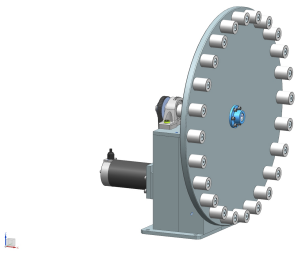

Figure 2.2: 3D rendering of the wheel.

A higher frequency signal modulation is suitable to improve the apparatus sensitivity. To this aim, a measurement with 24 masses on the wheel is planned and a high rotation stability is to be achieved. The spread of the angular velocity $\Delta\omega_{\text{wheel}}$ must be at least comparable with the one of the RLC circuit $\Delta\omega_{\text{rlc}}$, otherwise the sensitivity of the experiment will result limited. Since the resonant circuit quality factor is expected to be of the order of $Q \simeq 10^4$, the spread results $\Delta\omega_{\text{wheel}} = Q/\omega_0 \simeq 20\,\text{Hz}$ (considering a resonance frequency $\omega_0 \simeq 500\,\text{Hz}$). However, for the first sets of measurements, the smaller 4-teeth wheel was not stable enough to provide a good reference for the signal. A good integration with a phase detection scheme was not possible, so the wheel was equipped with 64 evenly spaced holes to achieve a good control on the modulation of the signal. This fine sampling of the rotation frequency allows

to remove noise from the signal using a lock-in amplifier; the details of this procedure are explained in Section 5.2.

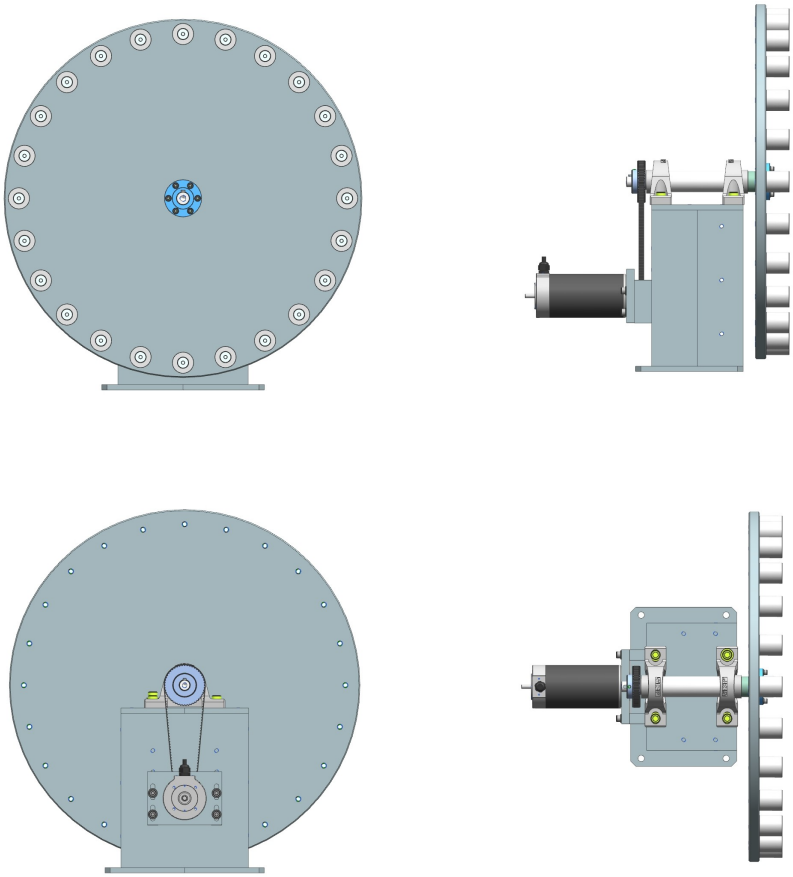

Figure 2.3: Different points of view of the wheel.

2.2 Detector

The paramagnetic sample is a cubic crystal of gadolinium oxyorthosilicate Gd_2SiO_5 (GSO) of 1 cm length [40]. Its features are reported in Table (2.1). Its magnetic properties will be described in detail in Chapter 3. The monopole-dipole interaction, acting on the electron spins in the crystal, causes a change in the magnetization of the sample and induces a change

of the magnetic flux collected by a coil surrounding the GSO. To reduce thermal fluctuations, the crystal is cooled down to cryogenic temperature ($T \simeq 4\,\mathrm{K}$). The distance between source and detector is 3.7 cm.

Volume	$V = 1\,\mathrm{cm}^3$
Mass	$6.71\,\mathrm{g}$
Density	$\rho = 6.71\,\mathrm{g/cm}^3$
Molar weight	$\rho_{\mathrm{mol}} = 422.58\,\mathrm{g/mol}$
Number of moles	$N_{\mathrm{mol}} = 0.015\,\mathrm{mol}$
Spin relaxation time	$\tau_M = 7.4 \cdot 10^{-11}\,\mathrm{s}$
Effective number of μ_B	$p_{\mathrm{eff}} = 8.02$
Magnetic susceptibility	$\chi_0 = 0.7$

Table 2.1: Summarized features of the used GSO crystal.

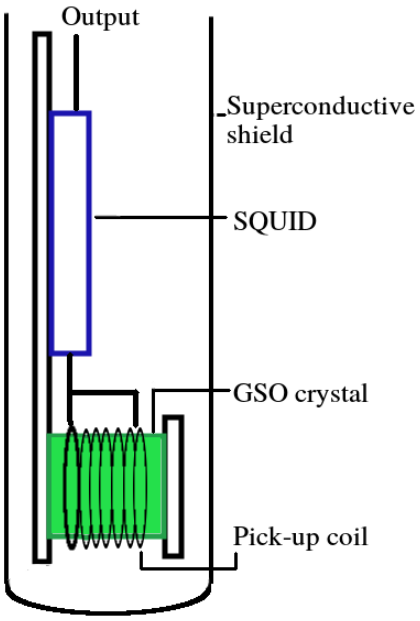

Figure 2.4: Scheme of the detector, the SQUID is represented as a in blue, while the GSO crystal in green.

It is worth noticing that B_{eff} is not subjected to Maxwell's equations. Therefore the sample can be shielded from electromagnetic noise sources without affecting the signal. For this purpose two MgB_2 superconductive shield are used to remove external noise of an expected factor 10^{12}. In addition, the apparatus is placed in a μ-metal cylinder that reduces the magnetic fields of an expected factor of the order of 10^2. The temperature was controlled through a Pt100 thermometer placed inside the superconductive shield, which was switched off at the moment of the measurement. The superconductive shields, however, freeze every DC magnetic field already present in their inside at the moment of the superconducting transition, such as the one of earth. This static magnetic field should not

be a problem, since it does not change the magnetic flux that is revealed by the SQUID (see subsection 2.3.3). This is true in absence of mechanical oscillations, in fact if the crystal moves inside a static magnetic field, the result is a magnetic flux through the pick-up coil at the frequency of the vibration, hence a possible background signal. Since the rotating wheel, for example, will move air surrounding the cryostat exactly at its rotational frequency, it has to be verified that this background signal does not affect the measurements, as it can be easily confused with the searched signal.

During the research and development phase of the experiment, it was taken in consideration the possibility of using a ferrimagnetic high-spin-density material as detector: Yttrium Iron Garnet (YIG) ferrite. Its high magnetic susceptibility increases the intensity of the signal, but, to achieve a better SNR, it has to be compared with the noise level. Since measurement of the magnetic noise of the YIG are not present in literature, the first measure of it has been done. This work was carried out together with M. Spagnol and is partially reported in his thesis "*Magnetization Measurement for Dark Matter Searches*". The results of this measurements will be reported in an article titled "*Measurement of the YIG magnetization noise*" which is in course of elaboration. The use of this ferrimagnet instead of the GSO was discarded because of the high magnetic noise level. This is discussed in details in Appendix C.

2.2.1 The cryostat

The cryostat that houses the GSO crystal is a liquid helium cryostat designed at the Padua section of the INFN and it's scheme is reported in Fig.(2.5). It consists subsequently in a liquid nitrogen chamber, a vacuum chamber and a liquid helium chamber, and can maintain the crystal at liquid helium (lHe) temperature for 7 hours, as calculated hereafter and reported in Fig.(2.6), where the slope of the straight line gives the evaporation rate. This feature of the cryostat is fundamental to achieve an integration time of several hours. Another important detail of the cryostat is the small distance which lies between the lHe vessel and the room, this guarantees the smallest possible distance between the source and the detector, crucial for the sensitivity of this experiment. The vacuum chamber reaches a pressure lower than 10^{-8} mbar in presence of liquid helium; this pressure level is approximately maintained during the acquisition.
The project of the cryostat is reported in Fig.(2.5), the most important thing to notice is the lower part of it, which allows the 3.5 cm distance between the source and detector centers of mass.

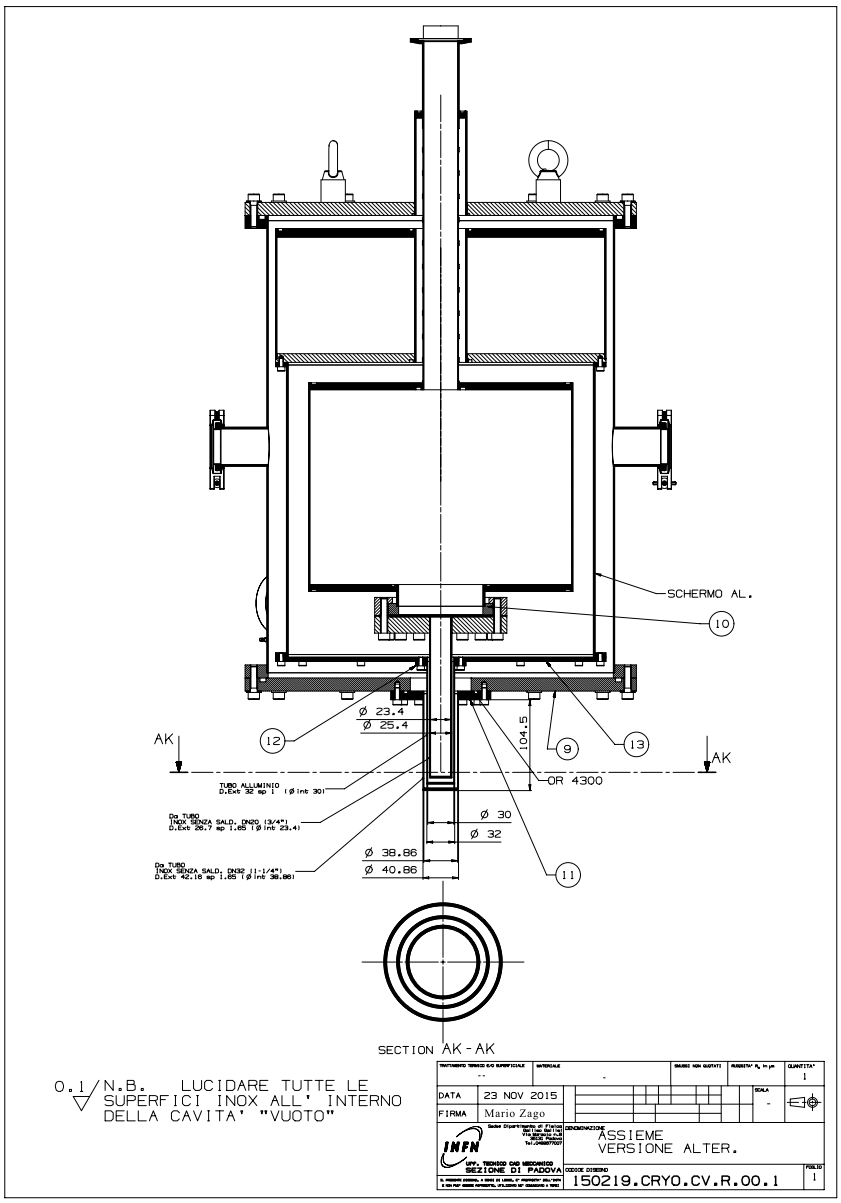

Figure 2.5: Lateral section of the liquid helium cryostat used in this experiment, which shows the lN, vaccum and lHe chambers. At the bottom a vertical section of the appendix is reported, notice that the 4 K chamber is close to the outside of the cryostat. Project by Mario Zago and Marco Romanato - Uff. Tecnico Meccanico - I.N.F.N sezione di Padova.

As previously hinted, some hour long integration time is essential to lower the random background noise. Fig.(2.6) shows the losses of the cryostat, that were estimated using a liquid helium level controller, used in low-noise mode not to affect the measurements of the SQUID. From the slope of the fitted line in Fig.(2.6) one can estimate an integration time 7 h, since the capacity of the cryostat is around 17 l and the evaporation rate of 2.4 l/h.

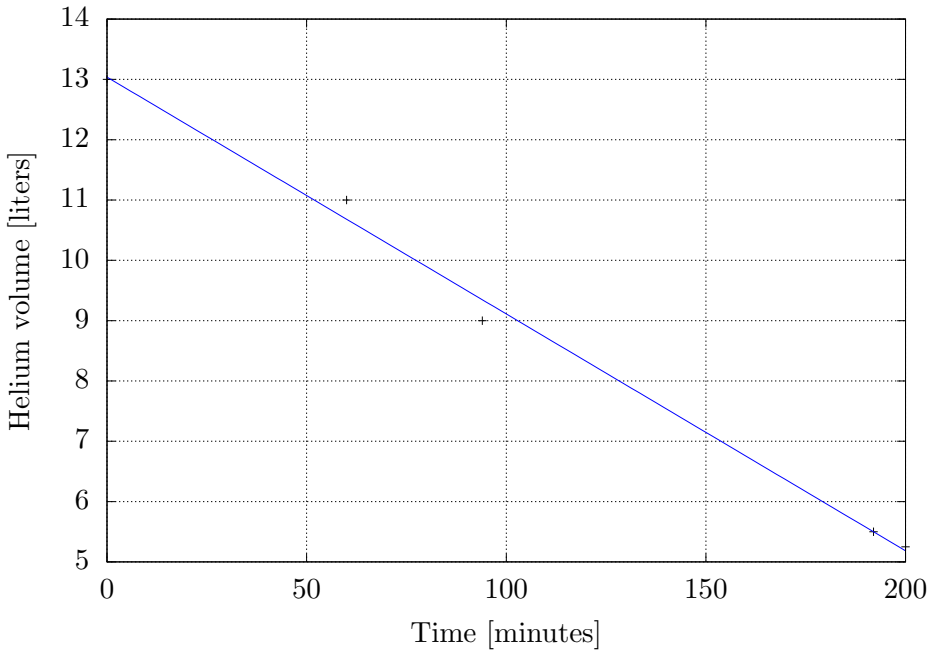

Figure 2.6: Estimation of the losses of the cryostat, needed to understand the possible length of the integration time of a single acquisition.

The vacuum chain is composed by a scroll pump VARIAN SH-100 used to produce the pre-vaccum, in series with a turboolecular pump Pfeiffer TMU261, that permits to reach the high vacuum range inside tha chamber of the cryostat. The pressure inside the vacuum vessel of the cryostat was controlled using both a Pirani Pfeiffer TPG201 and a Penning Edwards GP25-5 gauge. In addiction, it has been checked for leaks using a helium mass spectrometer. In order to limit the vibrations the cryostat was decoupled from the floor using high density rubber, placed below the suspension structure. This will damp the oscillations coming from the floor, nevertheless the SQUID is sensible enough to be affected also from acoustic vibrations.

2.3 SQUID readout

To detect the signal coming from the sample a SQUID based magnetometer is used. Its functioning principles are described in the following subsection (2.3.1), while in the next one (2.3.3) the readout is explained.

2.3.1 The dc-SQUID

The SQUID (Superconductive Quantum Interference Device) is a very sensible magnetometer based on superconducting loops containing Josephson junctions[1], in particular in this experiment a dc-SQUID is used [41].

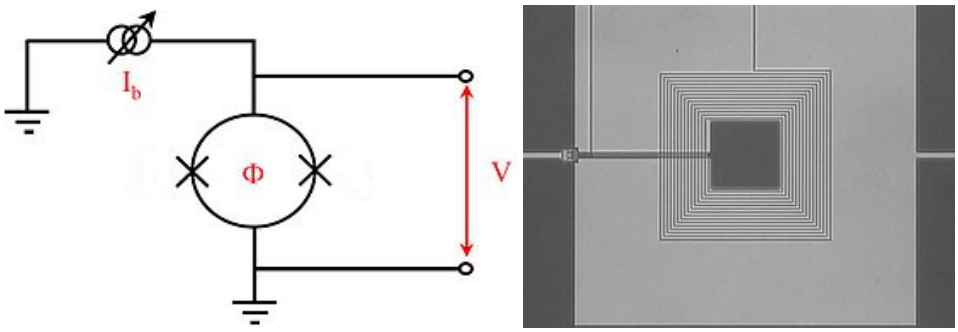

Figure 2.7: On the left side is reported the lumped element representation of the dc-SQUID: I_b is the bias current applied to the junction, ϕ is the magnetic flux and V is the voltage to be read. On the right side there is an image of an actual dc-SQUID superconducting loop.

This device combines the physical phenomena of flux quantization and Josephson tunneling. First predicted by F. London, flux quantization was observed experimentally by Deaver and Fairbank, and Doll and Näbauer in 1961. They showed that the flux contained in a closed superconducting loop is quantized in units of the flux quantum $\phi_0 = h/2e = 2.07 \times 10^{-15}$ Wb. Here, h is Planck's constant, and e is the electronic charge. It is based on the direct current Josephson effect. In the absence of any external magnetic field, the input current I splits into the two branches equally. If a small external magnetic field is applied to the superconducting loop, a screening current, I_s, begins circulating in the loop that generates a magnetic field canceling the applied external flux. The induced current becomes $I/2 + I_s$ in one branch and $I/2 - I_s$ in the other. As soon as the current in either branch

[1]The Josephson junction consists of two weakly coupled superconducting electrodes.

exceeds the critical current, I_c, of the Josephson junction, a voltage appears across the junction. Now suppose the external flux is further increased until it exceeds $\phi_0/2$. Since the flux enclosed by the superconducting loop must be an integer number of flux quanta, instead of screening the flux the SQUID now energetically prefers to increase it to ϕ_0. The screening current now flows in the opposite direction. Thus the screening current changes direction every time the flux increases by half integer multiples of ϕ_0, and the critical current oscillates as a function of the applied flux. The voltage in this case is thus a function of the applied magnetic field and the period equal to ϕ_0. Since the current-voltage characteristics of the dc-SQUID is hysteretic, a shunt resistance, R is connected across the junction to eliminate the hysteresis. This resistance is the source of the SQUID noise, discussed in Section 2.3.2.

2.3.2 SQUID noise

As reported in the SQUID Handbook [41], for a dc-SQUID (schematically reported in Fig.(2.8)), an estimation of the noise can be given starting from the technical data of the device.

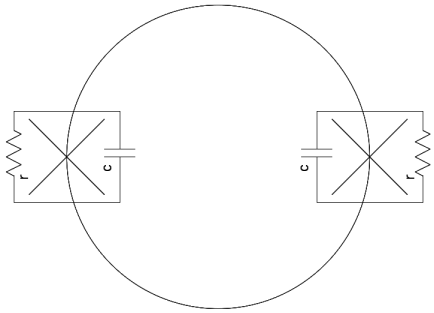

Figure 2.8: Scheme of the dc-SQUID, with schematic Josephson junction.

The interested noise is the one at the pick-up coil, and it's spectral density is given by

$$S_\phi^{(p)}(\omega) = \frac{(L_i + L_p)^2 S_\phi(\omega)}{M_i^2}, \tag{2.1}$$

where L_i and L_p are the inductances of the interior and pick-up coils, $S_\phi(\omega)$ is the spectral density of the flux noise and $M_i = k_i\sqrt{L_i L_l}$ is the mutual inductance of the interior coil coupled with L_l (the inductance of the loop).

The source of the noise is a Johnson-Nyquist current associated to a shunt resistance (R) used to remove the hysteresis of the Josephson junction. One can find that, under optimum conditions, the spectral density of the flux noise is

$$S_\phi(\omega) = 16 k_B T L_l^2 / R. \tag{2.2}$$

Combining Eq.(2.1) and (2.2) and considering a coupling k_i, one can easily find the spectral density of the equivalent flux noise at the pickup coil:

$$S_\phi^{(p)}(\omega) = \frac{(L_i + L_p)^2}{L_i L_p} S_\phi(\omega). \tag{2.3}$$

So the equivalent noise energy and then the magnetic field noise can be calculated in the minimum given by $L_i = L_p$,

$$\begin{aligned} \epsilon^{(p)}(\omega) &= \frac{S_\phi^{(p)}(\omega)}{2L_p} = \frac{(L_i + L_p)^2}{2L_p M_i^2} S_\phi(\omega) \\ &= \frac{4 S_\phi(\omega)}{2 k_i^2 L} = \frac{4\epsilon(\omega)}{k_i^2}. \end{aligned} \tag{2.4}$$

The pickup coil has a radius $r = 7.5\,\mathrm{mm}$ and $N = 8$, considering the features of the SQUID the noise energy $\epsilon(\omega) \simeq \hbar$ and an ideal coupling $k_i = 1$ one can find the magnetic field noise

$$\sqrt{S_B^{(p)}(\omega)} = \frac{\sqrt{S_\phi^{(p)}(\omega)}}{N(\pi r^2)} = \frac{\sqrt{8 L_p \epsilon(\omega)}}{N(\pi r^2)} = B_N / \sqrt{\Delta\nu}. \tag{2.5}$$

Where B_N is the equivalent noise field, this gives:

$$\sqrt{S_B^{(p)}(\omega)} = B_N / \sqrt{\Delta\nu} = 3.8 \cdot 10^{-18}\,\mathrm{T}/\sqrt{\mathrm{Hz}}. \tag{2.6}$$

As last check, using the nominal value of noise for the used SQUID (reported in the data sheet): $S_\phi^{1/2}(1\mathrm{kHz}) = 0.81\,\mu\phi_0/\sqrt{\mathrm{Hz}}$ with the same values used above and replacing them in Eq.(2.1):

$$\sqrt{S_B^{(p)}(\omega)} = B_N / \sqrt{\Delta\nu} = 9.2 \cdot 10^{-19}\,\mathrm{T}/\sqrt{\mathrm{Hz}}, \tag{2.7}$$

which is compatible with the previous calculation. To read current changes one must couple the input coil L_i with the internal inductance of the loop, the mutual inductance limits the sensitivity of the device to a 5% of the calculated value, with $M_i = 8.8\,\mathrm{nH}$. Therefore, using Eq.(4.4) and normalizing the flux for this pick-up coil, the calculation yields $(S_B^{(p)}(\omega))^{1/2} \simeq 7.3 \cdot 10^{-16}\,\mathrm{T}/\sqrt{\mathrm{Hz}}$.

2.3.3 SQUID calibration and electronics

An approximate calibration of any SQUID can be made using its V/ϕ characteristic, which is checked when the device is used. Data showing a typical example of this are reported in Fig.(2.9). When the dc-SQUID is biased

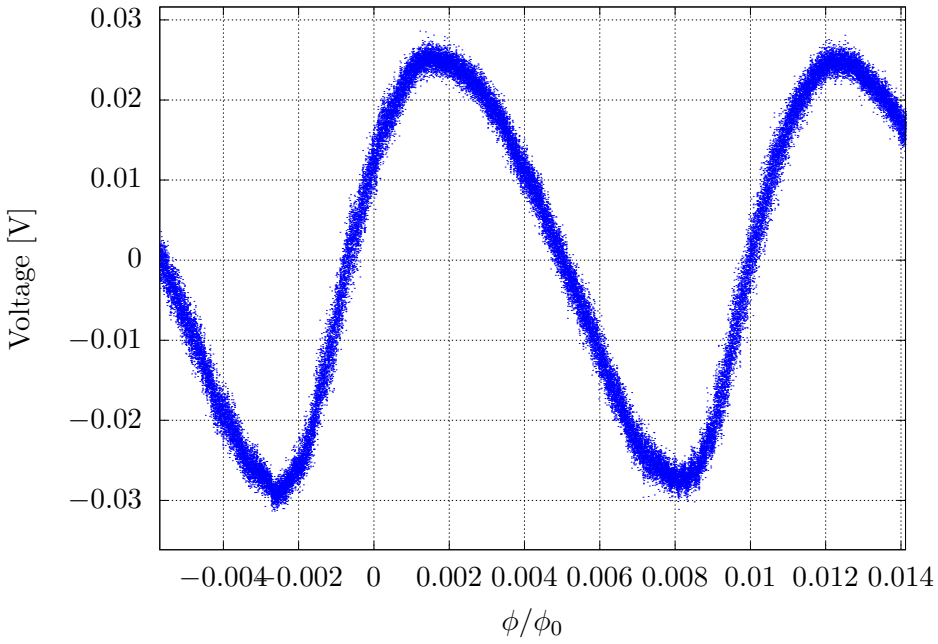

Figure 2.9: Tension vs. flux ϕ/ϕ_0 of a measurement.

at an appropriate constant current I_b , changes in applied magnetic flux cause the voltage to swing between two extrema, producing the oscillations with period ϕ_0 shown in Fig.(2.9). The maximum response to a small flux change $\delta\phi \ll \phi_0$ is obtained when $\phi_a \simeq (2n+1)\phi_0/4$, where the flux-to-voltage transfer coefficient $|\partial V/\partial\phi_a|$ is a maximum. This happens in in the interval where the slope of the sine is higher.

However, to have a more precise calibration, the pick-up coil of the SQUID was placed inside a controlled magnetic field. This was possible using a bigger coil L in which is placed the smaller pick-up coil. Than, using the signal generator reported in Fig.(2.10) a known magnetic field was generated into the coil at a chosen frequency. The generator allows to modify the voltage (e.g. the magnetic field) and the frequency of the signal, collected by the pick-up coil and read with a spectrum analyzer HP-35660A.

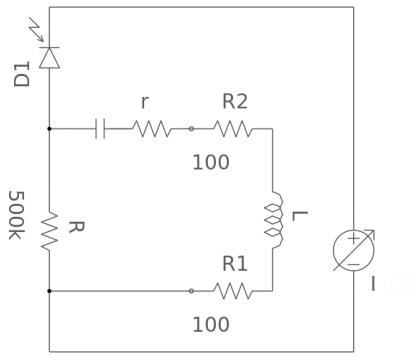

Figure 2.10: Lumped element circuit of the generator used for the calibration of the SQUID. Here L is the coil in which is placed the SQUID pick-up coil.

This permitted a precise calibration of the SQUID, as reported in Fig.(2.11).

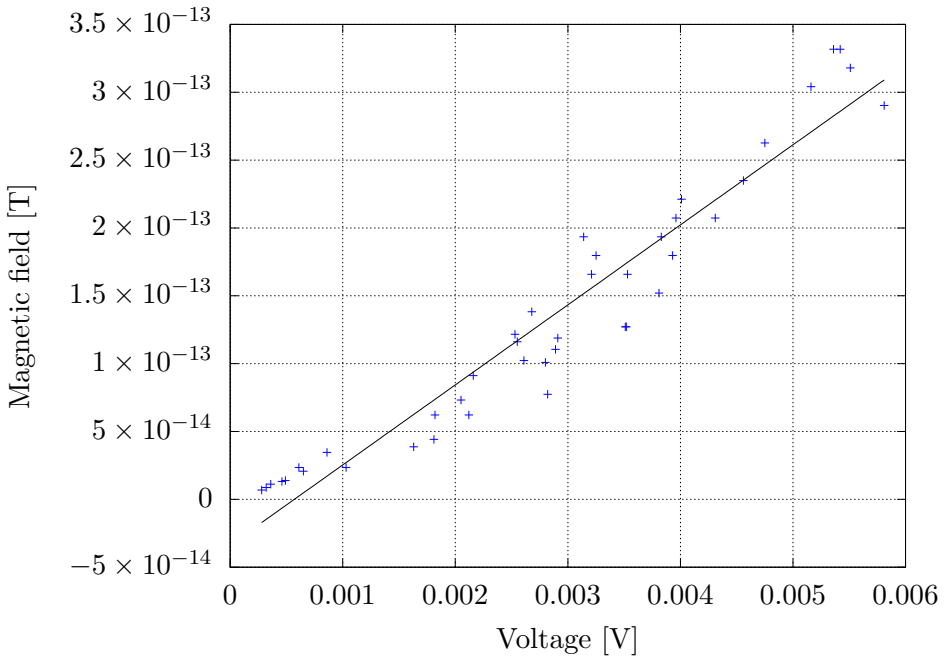

Figure 2.11: Calibration of the SQUID using the homogeneous magnetic field generated by the external coil L. The result is 4.2×10^{-11} T/V.

To measure the GSO magnetization induced by the source it is used a Magnicon C6XXL1W dc-SQUID. With reference to Fig.(2.12), the coil L_p picks up the magnetic flux generated by GSO magnetization; L_p is connected to the SQUID input coil L_i. Optimal work conditions of the SQUID require $L_p \simeq L_i$.

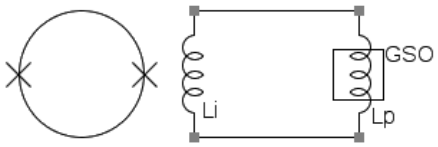

Figure 2.12: Lumped element model of the apparatus. $L_i = 1.8\,\mu$H is the input coil of the SQUID, $L_p \simeq 1.8\,\mu$H is the pick-up coil around the GSO crystal.

To further increase the sensitivity of the apparatus, the signal can be amplified with a resonant RLC circuit, tuned at the signal frequency, reported in Fig.(2.13).

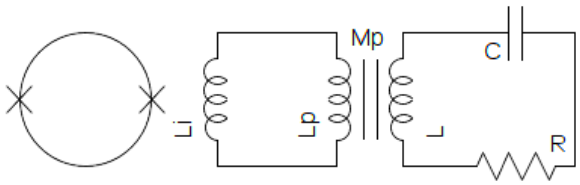

Figure 2.13: Lumped element model of the resonant pick-up circuits coupled with the SQUID through the mutual inductance M_p. The detector crystal is wrapped in the pick-up coil L_p as in Fig.(2.12).

The GSO crystal is still placed inside L_p as previously. The resistance R is an equivalent resistance accounting for all circuit losses, L is the inductance of the coil, C is the capacity, L_i is the internal inductance of the SQUID, L_p is the pick-up coil, and M_p is the mutual inductance between L_p and L. In the resonant readout configuration, the signal is increased by the Q-factor of the resonant circuit. The signal produced by this configuration will be analyzed in details in Section 5.2.2.

Chapter 3

GSO magnetic properties

The GSO (Gd_2SiO_5) is a paramagnetic crystal (whose magnetic proprieties were characterized by Baiboussinov, *et al.* [40]), that is going to be used in the QUAX-$g_p g_s$ experiment. For the aim of this experiment, the interesting properties of GSO crystals are the ones that affect signal and noise, i.e. magnetic susceptibility χ_0 and spin relaxation time τ_M. The sample is a cube-shaped GSO crystal, whose features are reported in Table (2.1). Here will be performed a theoretical calculation of his susceptibility, followed by two different experimental techniques of measurement.

3.1 Theoretical susceptibility

Assuming $k_B T \gg g\mu_B H$, where H is the external magnetic field, the susceptibility of a set of identical ions of angular momentum $J = L + S$ is given by Curie law

$$\chi_0 = \mu_0 \frac{N}{V} \frac{(g\mu_B)^2}{3} \frac{J(J+1)}{k_B T}, \tag{3.1}$$

where μ_0 is the vacuum magnetic permeability, N/V is the number of ions for unit of volume, g is the Landé factor, μ_B is Bohr's magneton, $J = L+S$ is the total angular momentum of the ion, k_B is Boltzman's constant and T is the temperature. When the free ions are part of a lattice in a solid structure, e.g. ions with partially filled electronic f-shells in insulating crystals, the generalized Curie law of paramagnetic susceptibility reads [42]

$$\chi_0(T) = \mu_0 \frac{N}{V} \frac{\mu_B^2}{3} \frac{p_{\text{eff}}^2}{k_B T}, \tag{3.2}$$

where p_{eff} is the effective number of Bohr magnetons. Here $p_{\text{eff}} = g\sqrt{J(J+1)}$, where g is the Landé factor

$$g(J,L,S) = \frac{3}{2} + \frac{1}{2}\Big(\frac{S(S+1) - L(L+1)}{J(J+1)}\Big) \tag{3.3}$$

taking the electron g_0-factor to be exactly 2.
Crystals containing rare earth ions (which have partially filled electronic f-shell), like gadolinium, obey the law in Eq.(3.2). In fact, for the Gd, the values found in literature are reported in Table (3.1). With this data, using

	Electronic configuration	p_{eff}	p_{mes}
Gd	$4f^7$	7.94	8.0

Table 3.1: Values of p_{eff} for Gd, the magnetic ion of GSO.

the features of these samples reported in Table (2.1), a first value of χ_0 can be calculated. Since $N = 2n \cdot N_a$ (where N_a is Avogadro's number, n is the number of moles of the sample and the factor 2 considers that there are two Gd atoms in a GSO molecule), the calculation yields

$$\begin{aligned}\chi_0 =& \frac{1}{3}\frac{N}{V}\frac{\mu_0\mu_B^2 p_{\text{eff}}^2}{k_B T} = \\ =& \frac{2}{3}\,\frac{0.015 \times (6\cdot 10^{23})}{10^{-6}\,\text{m}^3}\,\frac{(4\pi\cdot 10^{-7}\,\text{H/m}) \times (9\cdot 10^{-24}\,\text{J/T})^2 \times 8^2}{1.38\cdot 10^{-23}\,\text{J/K} \times 4\,\text{K}} \simeq 0.71\end{aligned} \tag{3.4}$$

This is a first approximated value of the magnetic susceptibility of the GSO, and will be compared with two experimental results.

3.2 Measured susceptibility

In this Section the magnetic susceptibility of GSO is calculated using different methods. First the results of [40] are used to make a first estimation of the magnetic susceptibility through a fit of the M/B curve for small fields. Than, using the data collected during the preliminary tests of the resonant circuit, a second value of χ_0 is obtained. This values will than be compared with each other and to the theoretical value calculated in Section 3.1.

3.2.1 From interpolation

Referring to [40], the magnetic susceptibility of GSO was measured in the field cooling mode for $H = 100\,\mathrm{Oe}$, and fitted with a Curie-Weiss law:

$$\chi_{\mathrm{cgs}}(T) = \frac{C}{T - \Theta}; \tag{3.5}$$

the resulting parameters of a linear fit of $\chi^{-1}_{\mathrm{cgs}}(T)$ are $C = 16.13(7)\,\frac{\mathrm{emu\,K}}{\mathrm{mol\,Oe}}$ and $\Theta = -8.9(2)\,\mathrm{K}$. In the measures reported in [40], one can notice that for small applied magnetic field the behaviour of the susceptibility is almost linear, the slope of the line gives the χ_0.
From the fit parameters one can obtain the number of Bohr's magnetons p_{eff} already used in Eq.(3.2), this article reports a value of $p_{\mathrm{eff}} = 8.02$. Using this parameter, the calculation is similar to the one performed in the previous chapter, and gives $\chi_0(T) = 0.72$, obtained for using the previously reported features of the crystal.

3.2.2 From resonance frequencies

An estimation of GSO susceptibility can be made using a resonant RLC circuit. The resonance frequency $\nu_0 = \omega_0/2\pi$ of the circuit is given by

$$\nu_0 = \frac{1}{2\pi\sqrt{LC}}, \tag{3.6}$$

using this relation it is possible to find out information about inductance and capacity.
This technique will be applied using the same RLC circuit with and without the GSO crystal placed inside the coil, with the same capacity the expectation is that the shift of the resonance is entirely due to the inductance. If L_e is the inductance of the empty coil and L_G is the inductance with the GSO filling all the coil,

$$L_e \propto \mu_0, \qquad L_G \propto \mu = \mu_0(1 + \chi_0); \tag{3.7}$$

therefore, from Eq.(3.6) one can obtain the ratio between the two resonance frequencies. The calculation yields

$$\frac{\nu_0^e}{\nu_0^G} = \sqrt{\frac{L_G}{L_e}} = \sqrt{1 + \chi_0}, \tag{3.8}$$

where the relation in Eq.(3.7) was used. Two spectra of the same RLC circuit was collected with and without the GSO crystal inserted in the coil.

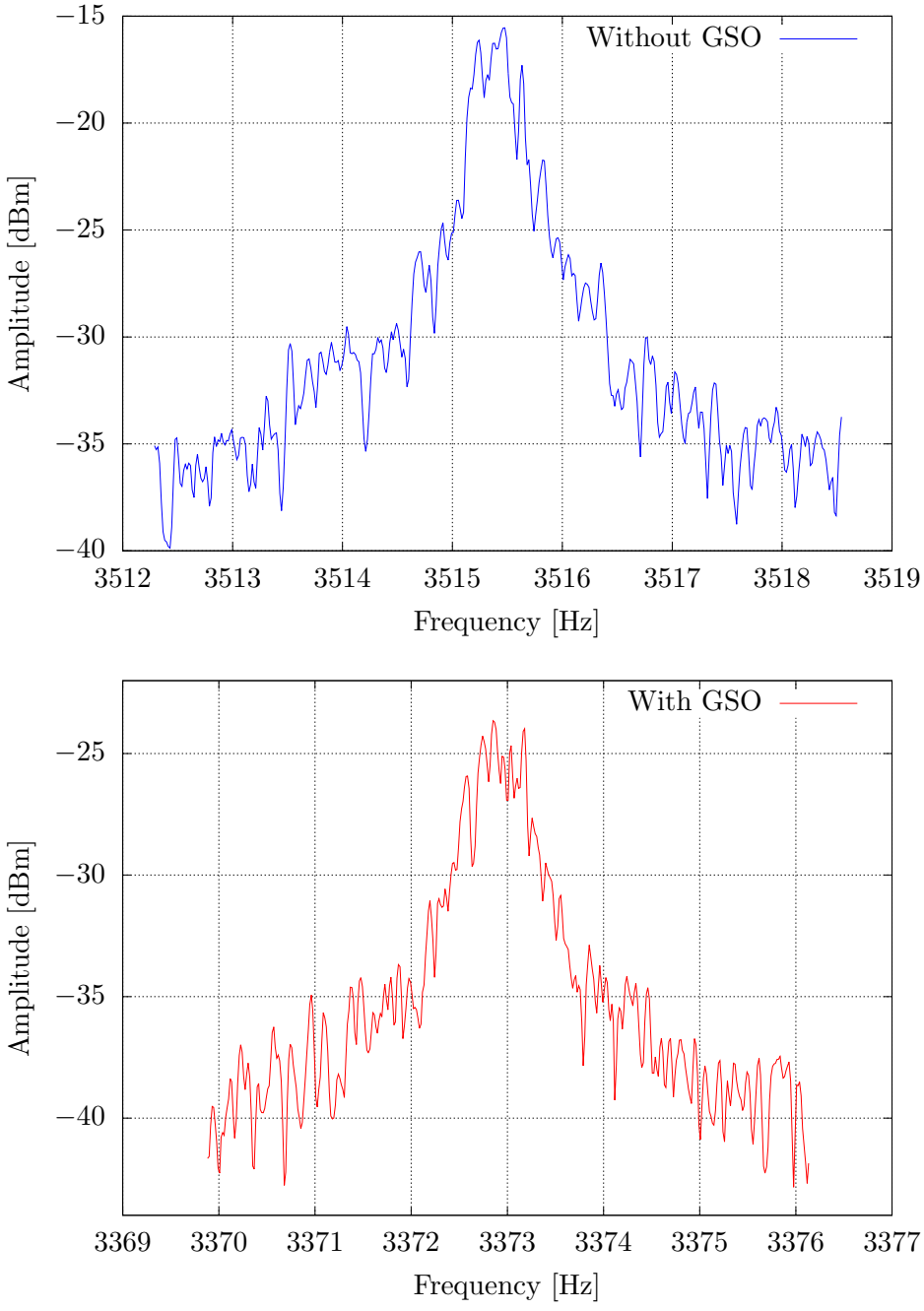

Figure 3.1: Graphics of the two resonances with GSO (red) and without GSO (blue).

Since all other parameters are the same, except for the two inductances it is possible to obtain the value of the susceptibility using the relation

$$\chi_0 = \left(\frac{\nu_0^e}{\nu_0^G}\right)^2 - 1. \tag{3.9}$$

The resonances are reported in Fig.(3.1) and the value of their resonance frequencies in Table (3.2). As expected there is a shift of the resonance frequency of about 140 Hz, probably due to the inductance, since nothing else was changed in the circuit. To find an estimated value of the magnetic susceptibility, it is possible to perform a calculation starting from experimental data reported in Table (3.2).

	Empty	With GSO
Capacity	150 nF	150 nF
Inductance	13 mH	15 mH
Resonance frequency	3.5154 kHz	3.3729 kHz
Quality factor	8788.5	4818.4

Table 3.2: Results of the calculations for the two cases.

This straightforward procedure however can not be applied directly to this case, since there are some differences to be taken into account.

Corrections

The previous calculation does not consider some corrections on the susceptibility:

1. multi-layered coil;
2. incomplete filling of the coil by the crystal;
3. effective number of electrons which give the magnetic moment.

This three factors will be taken into account in order to obtain a more precise value of χ_0.

1. **Multi-layer coil** - The 13 mH coil used is not made of a single layer of wire, so the formula to be used to calculate the inductance is

$$L = \mu \frac{0.8(R^2 N^2)}{6R + 9l + 10\Delta l}, \tag{3.10}$$

where μ is the magnetic permeability of the medium, R is the average radius, l is the length, N is the number of turns, Δl is the thickness of the coil. This will be taken into account in the following parts of the calculation, in fact Eq.(3.8) is no longer valid.

2. **Filling factor** - The geometry of the apparatus gives information about the region of the space filled by the crystal; in fact the coil is cylindrical, but the sample is cubic. Not all the space inside the coil is occupied by the GSO, but this geometry can be simplified considering an equivalent configuration, with two parallel cylindrical coils. The calculation in Eq.(3.11) takes into account this correction, using the parameter $\Theta(\chi_0) = (\nu_0^e/\nu_0^G)^2$.

$$\Theta(\chi_0) = \frac{L_G}{L_e} = \frac{\left(\frac{1}{L_1} + \frac{1}{L_2(1+\chi_0)}\right)^{-1}}{L_e}, \tag{3.11}$$

where L_1 is the external cylindrical empty coil, and L_2 is the internal coil (filled or not with GSO); the internal one is considered as an equivalent circular-based coil instead of one with a squared base, and L_e can be considerd L_1+L_2. A representation of this model is reported in Fig.(3.2).

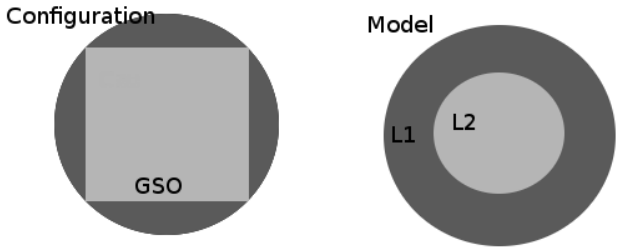

Figure 3.2: Schematic representation of the model used in the calculations.

Imposing $\Theta(\chi_0) = (3.5154/3.3729)^2 \simeq 1.086$ one obtains a value for the susceptibility $\chi_0 \simeq 0.7$.

3. **Effective magnetic moment** - The magnetism of GSO comes from the gadolinium ion, in which the magnetic moment is given almost entirely by the spin S. Referring to the first part of this section, in particular to Table (3.1) and Eq.(3.2), considering $J = L + S$, the χ_0 of the GSO measured for J is equal to the one for S, since J is almost

completely given by the spins. For this reason no correction has to be done.

After the corrections, the value of the susceptibility remains heavily approximate, however its final value $\chi_0 \simeq 0.7$ is compatible with the results obtained with the other procedures.

3.2.3 Imaginary part of the susceptibility

From the acquired data it is also possible to understand more about the imaginary part of the χ. In fact writing $\chi(\omega) = \chi'(\omega) + i\chi''(\omega)$, the two parts imply the presence of added resistance and inductance to the circuit:

$$L_a = 4\pi\xi L_e\chi', \qquad R_a = 4\pi\xi\omega L_e\chi''. \tag{3.12}$$

The first shifts the resonant frequency of the circuit, while the second modifies the damping and is a source of Johnson noise.
Using the difference between the quality factors of the circuits, one can give an estimated value of R_a (in fact a generic $Q = \omega_0 L/R$). In this case R is the resistance due to contact and losses, and the changing from $Q_e \to Q_G$ (using the previous subscripts) allows the calculation of R_a and therefore of χ''. All the used values are reported in Table (3.2).

$$\begin{aligned} &Q_e = \omega_0^e L_e/R_e, \qquad Q_G = \omega_0^G L_G/R_G; \\ &R_a = R_G - R_e = 0.01\,\Omega - 0.005\,\Omega = 0.005\,\Omega; \\ &\chi''(\omega_0) = \frac{R_a}{4\pi\omega_0\xi L_G} = \frac{0.005\,\Omega}{4\pi \times 0.14 \times 3372.9\,\mathrm{Hz} \times 15\,\mathrm{mH}} \simeq 5.6 \cdot 10^{-5}. \end{aligned} \tag{3.13}$$

Which, at the resonance frequency, is much smaller than the real part of the susceptibility.

3.2.4 Summary

In the previous chapter were obtained three different values of the magnetic susceptibility of the GSO, these results are reported synthetically hereafter.

	Curie's law	Interpolation	Resonance
χ_0	0.71	0.72	0.7

Chapter 4

Noise and sensitivity

The tests of the various components were performed in a lHe dewar with a temporary apparatus, similar to the final one. After that, the first measurement inside the cryostat were performed. In this chapter both of them are reported. The aim was to identify the main source of noise, measure the actual background and compare it with the calculated one, in order to estimate the real sensitivity of the experiment.

To calculate the thermodynamic fluctuation of the magnetization, one has to resort to the fluctuation-dissipation theorem [43], which reads

$$S_M(\omega) = \frac{2k_BT}{\mu_0 \omega V} \mathrm{Im}(\chi(\omega)), \tag{4.1}$$

where $S_M(\omega)$ is the spectrum of the magnetization noise, and $\mathrm{Im}(\chi(\omega))$ is the imaginary part of the Fourier transform of the susceptibility. In the Debye approximation [44], and assuming $\omega\tau_M << 1$ one obtain

$$\mathrm{Im}(\chi(\omega)) = \mathrm{Im}\Big(\frac{\chi_0}{1 + i\omega\tau_M}\Big) \simeq \chi_0 \omega \tau_M. \tag{4.2}$$

Hence, the mean square fluctuation of the magnetization, integrated over a frequency band $\Delta\nu$, is

$$\sigma_M^2 = \int_{\Delta\nu} S_M(\nu) d\nu = \frac{4k_BT\chi_0\tau_M(\Delta\nu)}{\mu_0 V}. \tag{4.3}$$

To evaluate this quantity, the spin relaxation time τ_M of GSO was measured through an EPR spectrum, obtained with a ELEXSYS 580 Bruker instrument, equipped with a dielectric cavity at 80 K. The measurement gives a

linewidth $\Delta H_{pp} = 0.48\,\mathrm{T}$. Considering the gyromagnetic ratio of the electron γ_e, the calculation yields $\delta\nu = \gamma_e \Delta H_{pp} = 13.5\,\mathrm{GHz}$. Since $\gamma_e/2\pi = 28.0\,\mathrm{GHz/T}$ and $\tau_M = 1/(\pi\delta\nu)$, the spin relaxation time is $7.4 \times 10^{-11}\,\mathrm{s}$. Assuming no variation of τ_M from 80 K to 4 K the value of the noise depends only on the temperature; in this case $T \simeq 4\,\mathrm{K}$, and using the previously calculated $\chi_0(4\,\mathrm{K})$, the level of magnetization noise is $S_B^{1/2}(\omega) = 1.2 \times 10^{-16}\,\mathrm{T}/\sqrt{\mathrm{Hz}}$. A comparison between $S_B^{1/2}(\omega)$ and the SQUID noise calculated from Eq.(4.3) shows that their value is similar, therefore a detailed analysis of the two is needed.

4.1 Characterization of the main noises

The orders of magnitude of the magnetic noise and of the SQUID noise, Eq.(4.3) and Eq.(4.4) respectively, are comparable. In order to verify that the SQUID noise is above the magnetic noise, two measurements has been made. The first with GSO and the second without the crystal, both of them are reported in Fig.(4.1).

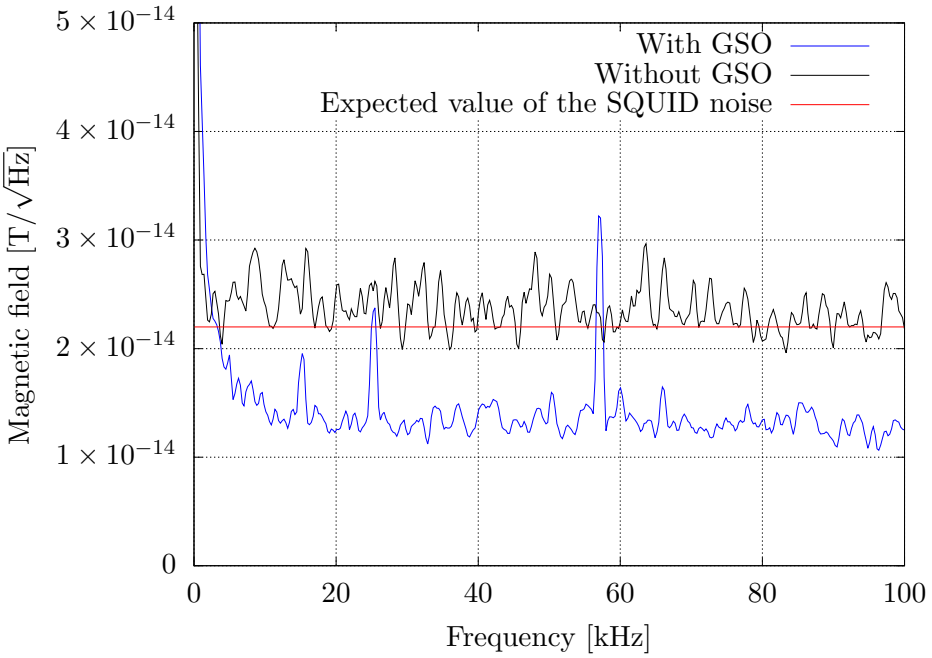

Figure 4.1: Measurement with and without the GSO into the pick-up coil, taken inside the test dewar. The red line represent the expected noise.

The spectrum reported in Fig.(4.1) allows to verify that the noise measured is the one of the SQUID. In fact, as discussed in Section 2.3.2, the optimal work conditions of the SQUID are reached if $L_p = L_i$ and in this case the condition is verified when L_p is filled by the crystal. In other words this relation is satisfied for the inductance of the coil wrapped around the GSO, the inductance of the empty coil changes as the magnetic permeability does ($\mu \to \mu_0$). This change of inductance forces not to work in optimal conditions, as a result, the SQUID noise increases. Assuming that the noise measured with the GSO is due to the SQUID, the new noise level can be estimated and compared with data. Since the two are compatible, it is possible to conclude that the main noise is actually due to the SQUID.

One last check can be made in order to verify that the noise is actually uncorrelated and random. Performing a vector averaging of the noise, using the internal reference of the analyzer as phase signal, is a technique to do it. A vector average takes into consideration the phase of the signal, allowing to remove the noise which is not in-phase with the signal. The measurement is reported in Fig.(4.2).

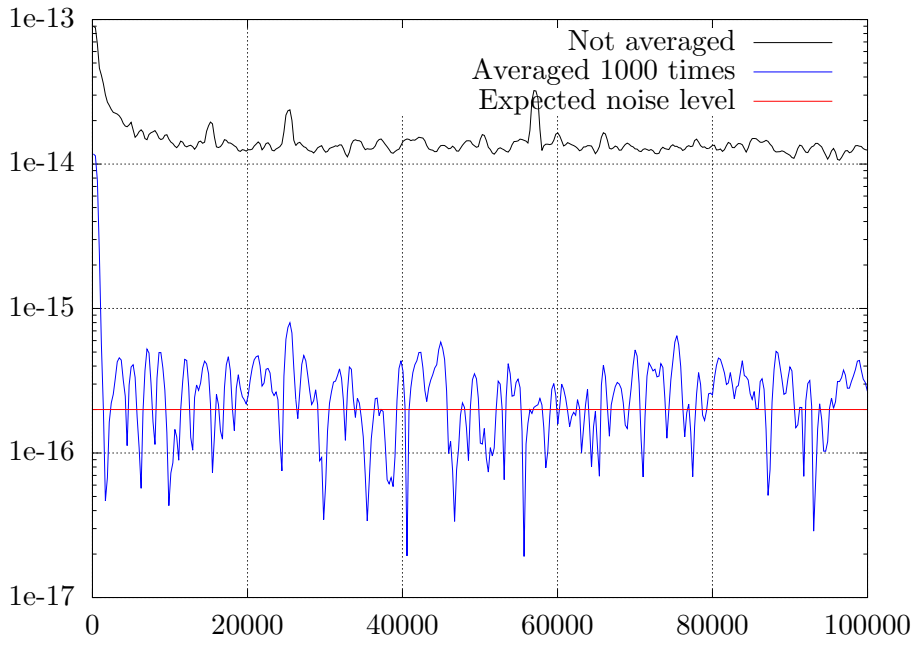

Figure 4.2: Phase-sensitive averaging over the background inside the test dewar. The reduction of the background is compatible with the expectation.

The figure shows that the integration reduces the background level of a factor $\sqrt{N} \simeq 100$, where N is the number of averages. This is exactly what was expected, since the considered noise has a random phase.

4.1.1 Demagnetization factor

The effect of the geometry of the sample in a magnetic field is quantified by the demagnetization factor: different shapes have different degrees of shearing, this is due to demagnetization fields. Maxwell's equations states that $\boldsymbol{B}$ must be continuous, but $\boldsymbol{H}$ is discontinuous at the surfaces of a finite object, with normal components $\boldsymbol{M}$. In this way, the surfaces acts as free poles. In principle this effect should limit the sensitivity of the experiment, however, this will be not taken into consideration, since the equivalent field induced by axions does not respect Maxwell's equations. What could be considered is the interaction of spins with the other spins surrounding them, in fact this interaction is independent on the nature of the force. However this is a second order correction and will therefore be considered negligible.

4.2 Noise measurements

The results of Eq.(4.3) and the measures of Section 4.1 suggest that the dominant noise of the experiment is the one of the SQUID. A detailed derivation of this noise is can be found in Section 2.3.2, here only the most important results and calculations are reported. Referring to Fig.(2.12), the spectral density of the equivalent flux noise at the pickup coil of the SQUID is given by

$$S_B^{(p)}(\omega) = \frac{1}{(n\pi r^2)^2} \frac{(L_i + L_p)^2}{M_i^2} S_\phi(\omega), \tag{4.4}$$

where n and r are the number of turns and the radius of the pick-up coil respectively, L_p is the pick-up coil inductance, L_i is the internal inductance of the SQUID, and $M_i = k\sqrt{L_s L_i}$ is the mutual inductance between L_i and the loop inductance of the SQUID L_s. The intrinsic SQUID flux noise level is $S_\phi^{1/2}(\omega) \simeq 0.81\,\mu\phi_0/\sqrt{\text{Hz}}$ [45], since $M_i = 8.8\,\text{nH}$ and $\phi_0 \simeq 2 \times 10^{15}\,\text{Wb}$, using Eq.(4.4) and calibrating the magnetic flux through the pick-up coil, the calculation yields $S_B^{(p)}(\omega)^{1/2} \simeq 7.3 \times 10^{-16}\,\text{T}/\sqrt{\text{Hz}}$.
As was determined in Section 4.1 this is the main noise of the experiment. Assuming that no ALP will be found, this values will be close to what will be obtained with the acquisitions. Under this assumption this backgrounds allow to give a first estimation of the $g_p g_s$ limit measured.

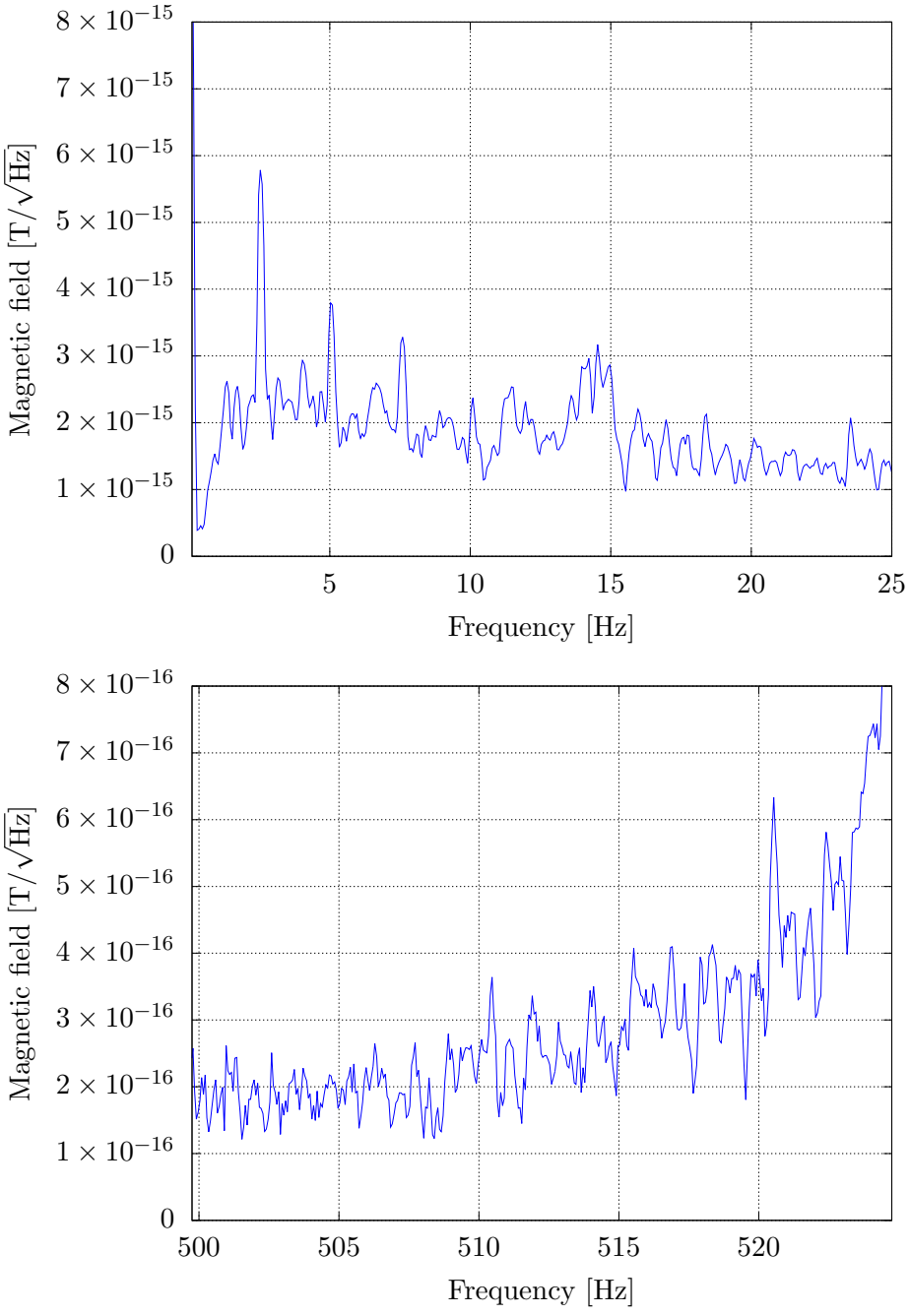

Figure 4.3: Square root of magnetic noise power density $\sqrt{S_B(\omega)}$ in the frequency bands of $g_p^e g_s^N$ measurements.

Noise spectra has been measured at frequencies $f > 0.1\,\mathrm{Hz}$ (i. e. above the $1/f$ noise knee of the SQUID [45]), and are reported in Fig.(4.3). As can be seen, there exist frequency bands where the background is compatible with the SQUID noise. The spectra are shown in the frequency bands of planned $g_p^e g_s^N$ measurements: around 10 Hz and 500 Hz. These measures are taken with a band-pass filter around the chosen frequencies. The intensity of the low frequency spectrum is slightly higher than expected, probably because of $1/f$ noises or vibrational noises.

4.3 Sensitivity calculations

The signal to be measured is a change of the GSO magnetization. For a paramagnet, the change of magnetization $\boldsymbol{M}$ due to an external field $\boldsymbol{H}$ is given by $\boldsymbol{M} = \chi_0 \boldsymbol{H} \equiv \chi_0 \boldsymbol{B}/\mu_0$, where χ_0 is the magnetic susceptibility. Likewise, the axion effective magnetic field will induce a change in the magnetization $\mu_0 M = \chi_0 B_{\mathrm{eff}}$, that will be collected by the pick-up coil. The noise sources are the magnetization noise and the SQUID noise; however, in this experimental apparatus the dominant noise is due to the SQUID as discussed in Chapters 3 and Section 4.2.

In order to obtain the signal generated by the source one has to start from the potential in Eq.(1.17), that is a single particle effective magnetic field. To get the intensity of the signal generated by a macroscopic body, an integration over the volume of the source is needed, calling V the volume of the mass and N the number of nucleons and $n = N/V$ the nucleon density of the bulk mass

$$\chi_0 S_B^{1/2} = \int_V n \boldsymbol{B}_{\mathrm{eff}}(\boldsymbol{r}) dV. \tag{4.5}$$

Here the signal is considered independent on time. For a first approximation the signal will thus be a squared wave whose value is the result of the integration of Eq.(4.5) when the source is in front of the detector and zero otherwise. This is possible also because in the calculation, due to the small dimension of the sample (compared to the source masses), it will be considered a point, that implies that inside the detector the field is considered to be uniform. This also implies that the source, seen from the detector, is like an infinite plane. Also if this seems a heavy approximation that could bring to a sensitivity higher than the real one, a more precise calculation, reported in Appendix D yield that this approximation works well in this case. In fact, thanks to the exponential decay, the intensity of the interaction falls quickly

with the increasing of r.
The explicit expression of the integral in Eq.(4.5) is

$$\int_V n\boldsymbol{B}_{\text{eff}}(\boldsymbol{r})dV = -\frac{\hbar^2 g_p^e g_s^N}{8\pi e\mu_B}\int_V n\hat{\boldsymbol{r}}\Big(\frac{1}{r\lambda_a}+\frac{1}{r^2}\Big)e^{-\frac{r}{\lambda_a}}dV, \tag{4.6}$$

applying the approximations discussed above and considering that n is constant over the volume, the integral becomes

$$\int_V n\boldsymbol{B}_{\text{eff}}(\boldsymbol{r})dV = \frac{\hbar^2 g_p^e g_s^N}{4e\mu_B}n\lambda_a(1-e^{-\frac{d}{\lambda_a}})e^{-\frac{z}{\lambda_a}} \simeq \frac{\hbar^2 g_p^e g_s^N}{4e\mu_B}n\lambda_a e^{-\frac{z}{\lambda_a}}, \tag{4.7}$$

where d is the depth of the source mass.
As is clear form Eq.(4.7), as the distance between the two centers of mass z increases, the intensity of the signal decreases and the correction due to the depth of the source is negligible. This value of will be used in the following section to estimate the sensitivity of the experiment.

Non-resonant readout

The signal to noise ratio of the magnetization measure is $\text{SNR} = \chi_0 B_{\text{eff}}/\sigma_B$, where $\sigma_B^2 = S_B^{(p)}(\omega)/t$ is the variance of the measure and t is the integration time. The minimum detectable magnetization at unitary signal-to-noise ratio corresponds to an equivalent field

$$B_{\text{eff,min}} = \frac{S_B^{(p)}(\omega)^{1/2}}{\chi_0\sqrt{t}}. \tag{4.8}$$

Substituting for the measured values of χ_0 and $S_B^{(p)}(\omega)$, and assuming an integration time $t \simeq 4\,\text{h}$, one gets $B_{\text{eff,min}} \simeq 10^{-17}\,\text{T}$. The present configuration of QUAX-$g_p g_s$ should be able to improve the upper limit reported in reference [46] of one order of magnitude.

Resonant readout

To further improve the sensitivity, a resonant pick-up circuit is exploit. Calculations in Appendix B show that the SNR is increased by $2Q$, where Q is the quality factor of the resonant circuit. Using the measured values of the non-resonant readout and $Q \simeq 10^4$, from Eq.(4.8) it is possible to estimate an effective field $B_{\text{eff,min}} \simeq 10^{-22}\,\text{T}$.
In Fig.(4.4) is summarized the expected sensitivity of the apparatus in terms

of the strength of the monopole-dipole interaction, compared with the upper limits already reached by other experiments. The measurements of other authors are reported in references [34, 36–39, 46–51]. It is worth mentioning that some experiments has been proposed [52, 53] that should be able to reach sensitivities of the same order of magnitude of this experiment.

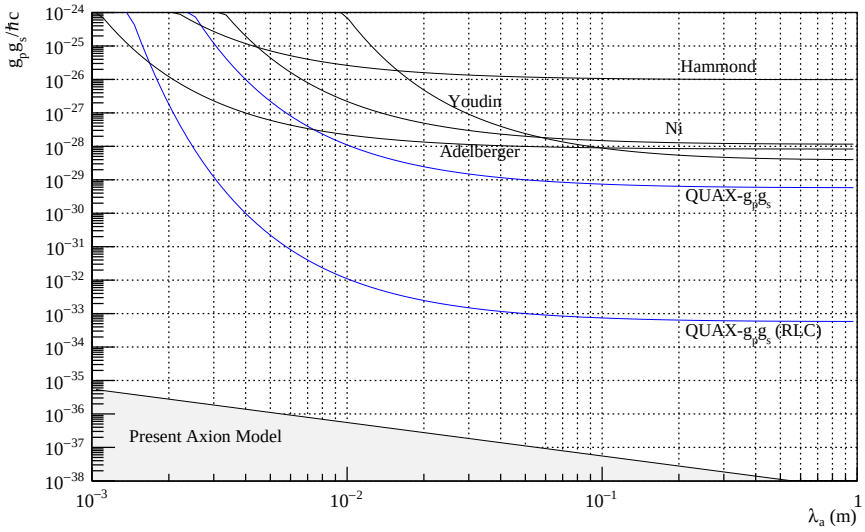

Figure 4.4: Expected sensitivity of QUAX-$g_p g_s$ with an integration time of 4 h. As can be seen the limit on the $g_p^e g_s^N$ coupling can be lowered of 1 or 5 orders of magnitude in the non-resonant or resonant (RLC) configuration, respectively. This figure also shows the $g_p^e g_s^N$ upper limits already reported in literature (see text).

Chapter 5

Measurements and data analysis

After the tests performed on the different parts of the experiment reported in the previous sections, the final apparatus was built as it is described in Section 2. The procedure usually starts the day before the actual measurement, when the outer chamber of the cryostat is filled with liquid nitrogen and a pre-vacuum is obtained using a scroll pump. After the pre-vacuum is created, the turbomolecular pump is switched on, this permits to reach a pressure around 10^{-7} mbar in a few hours. The next day, with the a steady vacuum and after refill of liquid nitrogen, the liquid helium (lHe) transfer can be made, the presence of lHe permits to reach a pressure below 5×10^{-8} mbar, which is the limit of the Penning vacuum gauge used for the pressure measurent. The actual pressure is probably on the order of 10^{-8} mbar, due the turbomolecular pump and to the condensation provided by lHe, no precise measurement have been made, since this parameter does not affect the signal.
To allow the integration of the signal provided by the spectrum analyzer, a reference (phase) signal is needed. A first effort to provide this phase signal was made using a reflective surface placed on the source masses and an opaque surface where there were no sources. Than, hitting with laser light the wheel and placing a photodiode to detect the reflected signal (see Fig.(5.1)), it is possible to obtain a signal in phase with the presence of the mass in front of the detector. The signal coming from the photodiode is almost a square wave and, once passed through a generator used to provide a suitable TTL signal, is sent to the analyzer to be used as external reference. This should allow the analyzer to integrate the signal using this phase.

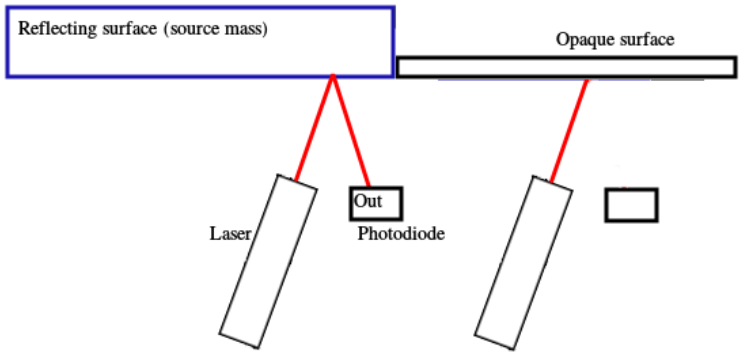

Figure 5.1: Schematized representation of the part of the apparatus used to obtain the phase of the searched signal. This scheme presents two states: the first, in a time when the signal arrives to the photodiode (left), and the second, in another time when it does not (right). This provides the time-modulation of the signal.

Unfortunately, since the phase signal provided by the wheel was not stable enough, this method does not allow a good integration of the signal. In fact as previously said, for the non-resonant measurement, a prototype wheel was used, which balance and stability have not been optimized. The solution of this problem was to use a different method to acquire the phase: 64 holes evenly spaced on the circumference of the wheel were made. Than, using a laser and a photodiode, it was possible to check the angular velocity ω as precisely as needed. The configuration is represented schematically in Fig.(5.2). This fine sampling of the rotation (and tough of the frequency), permits to lock the phase with a precision dependent on the number of holes

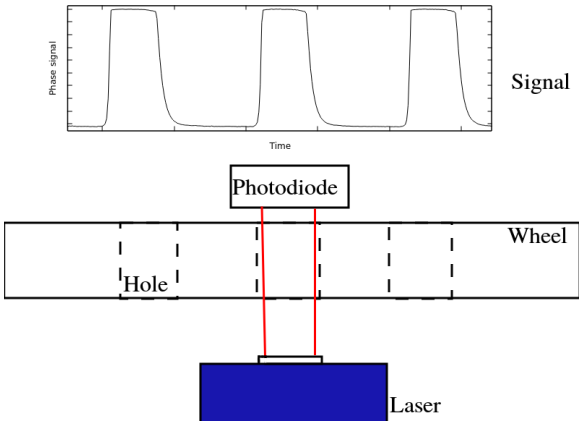

Figure 5.2: Fine sampling of the rotational frequency, see text for details.

in the wheel, in this case 64 samples per turn resulted enough. This expedient permitted to acquire two different signals, that will be processed via software, providing a phase-sensitive detection that will be explained in details in Section 5.2. The first test made on the final apparatus was for external noises. In fact it is not evident that the wheel, rotating outside the cryostat, does not affect the measurement. This is a reasonable doubt, also because the possible noise (due to air moved by the teeth or other vibrations) would be exactly in phase with the searched signal. In Fig.(5.3) the two measures taken, with the wheel on and off, are reported.

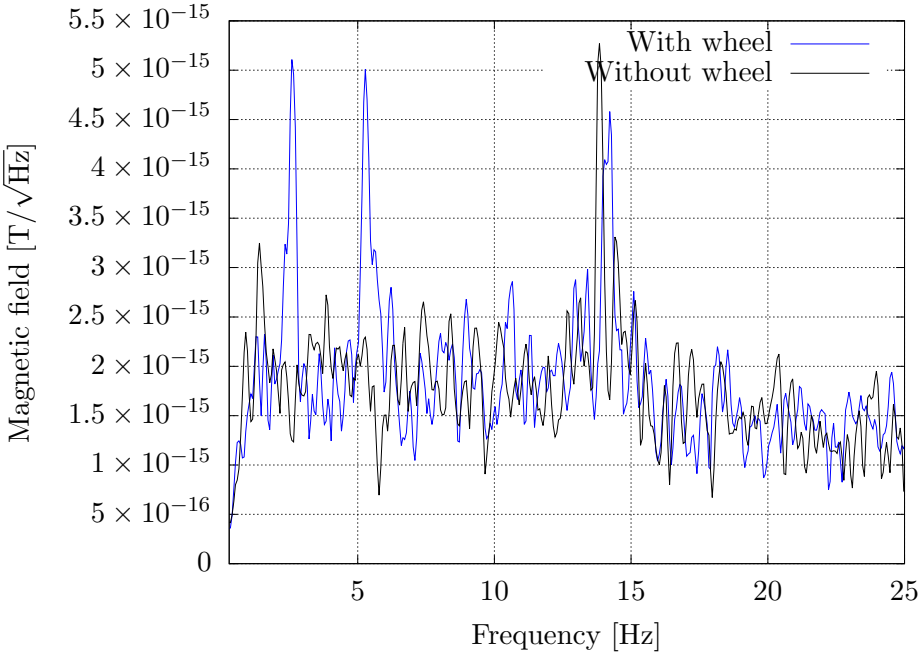

Figure 5.3: Comparison between the two spectra with and without the rotating wheel, the cut of the lowest frequencies is due to a band-pass filter.

As can be noticed, two sharp peaks are present in around 2 and 5 Hz, this are probably due to mechanical resonances of the structure of the wheel. In the other frequency bands the rotation seems not to disturb the signal, since the two background are compatible. Therefore the two peaks can be ignored[1] since they are distant from the 10 Hz planned for the measurement.

[1] However, in Section 6.1, a method to remove this noise is described.

5.1 Acquisitions

The first spectra with all the parts of the apparatus set-up and working were acquired to verify the presence of external noises affecting the signal. An example of acquisition is reported in Fig.(5.4).
As can be seen, differently from the first run of measurements, the background is lacking of vibrational peaks and external noises of various sources. This is probably due to the relaxation of the mechanic structures of the apparatus, after the first measurements at cryogenic temperatures. This background is close to what expected, confirming the possible result anticipated in Section 4.3. This data were used only as check before going on with the actual measure.

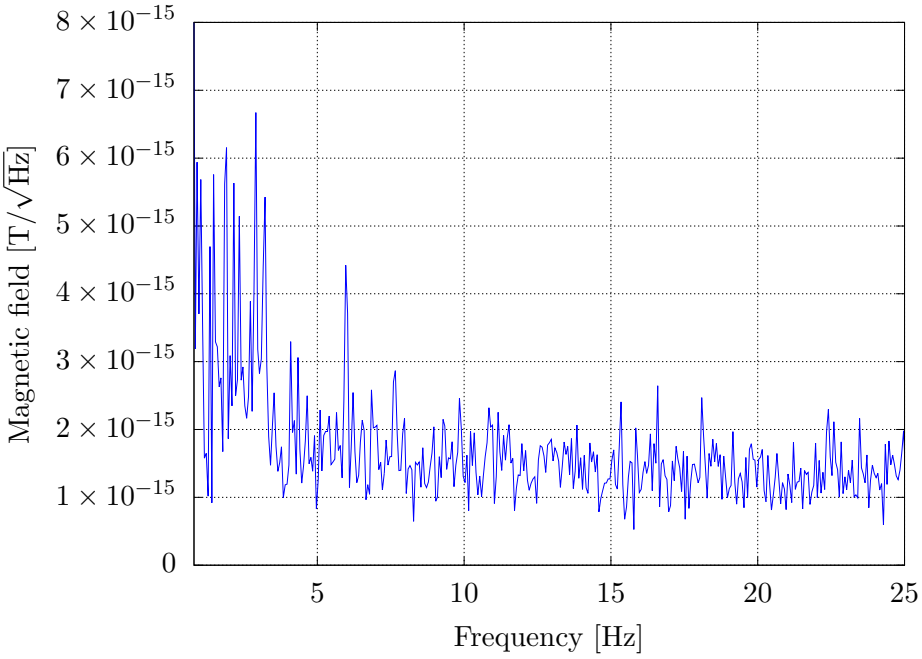

Figure 5.4: Background spectrum of the first acquisition with all the apparatus working. This spectrum is averaged 5 times using RMS averages.

It is worth noticing that at higher frequencies the background signal of the SQUID is lower of almost an order of magnitude, this is useful also without the resonant circuit. In fact, using an engine that allows a frequency $\omega \simeq 25\,\text{Hz}$ with a 24-teeth wheel, one can improve the measurement of

a factor 10. A spectrum around the frequency of 500 Hz is reported in Fig.(5.5), this is the planned resonance frequency of the RLC circuit and therefore of the resonant measures.

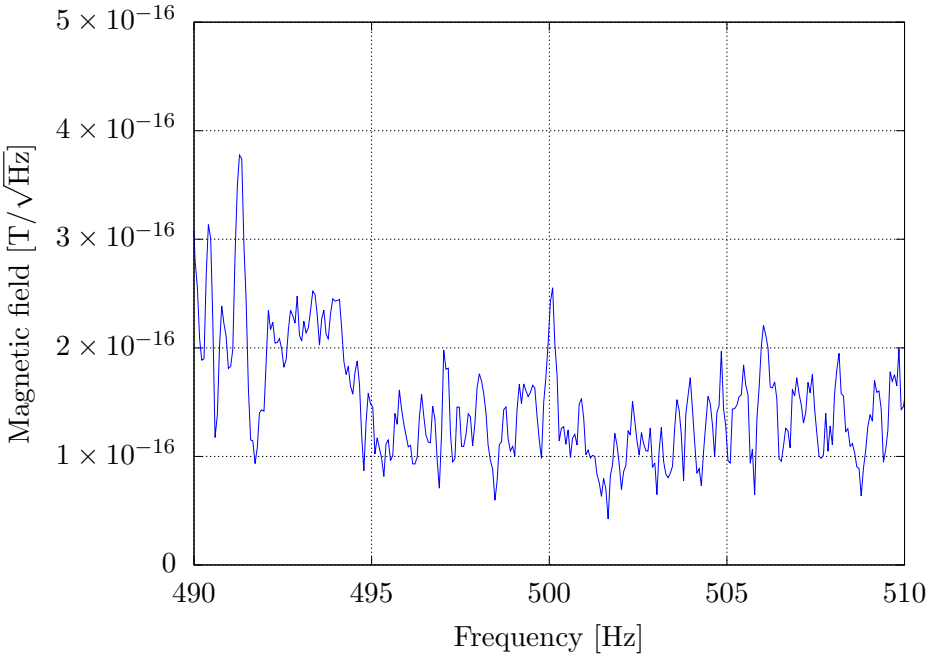

Figure 5.5: Background spectrum of the first acquisition with all the apparatus working. At higher frequencies the SQUID noise level is lower.

As was discussed, an integration using the phase of the wheel as TTL reference for the analyzer was not a useful solution for the reduction of the background. The actual measurements were thus made using a LeCroy HDO6000 high definition oscilloscope, the calibration of the SQUID, read by the oscilloscope, is made using the internal generator of the device and yield a value of 9.9×10^{-13} T/V. An acquisition consists in the two components described in the previous section, hereafter referred as signal and phase, briefly summarized below:

- *signal*: it have its origing in the GSO, is collected by the pick-up coil and read SQUID. Finally acquired by oscilloscope for a time of ~ 4 h;
- *phase*: it comes from a laser which supervise the angular speed of the wheel, is collected by a photodiode and eventually acquired by the same oscilloscope.

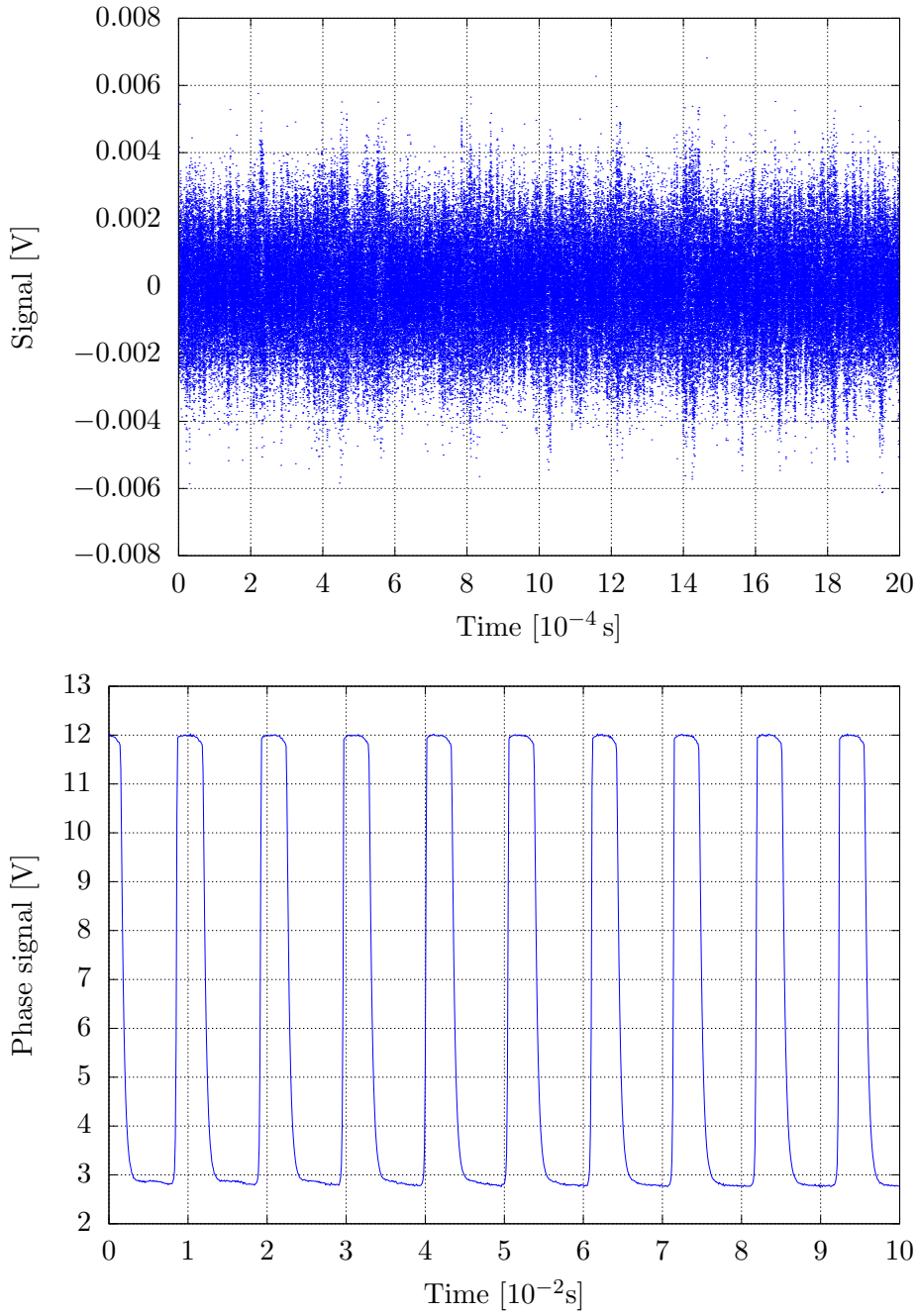

Figure 5.6: Part of the signal collected during first measurement with the oscilloscope, the upper plot is the signal, while the lower is the phase.

5.2 Analysis

Here will be performed two different types of analysis, since the resonant configuration need a more detailed procedure. The definitive measures with the resonant configuration are still to be made, so the following consideration regard the prototype wheel and therefore the oscilloscope analysis. It is still not certain if this acquisition system will be used also for the resonant measures, since the more stable wheel should allow a good TTL signal used as reference for a spectrum analyzer. Section 5.2.1 essentially describes the software used for the signal-phase acquisition, while in Section 5.2.2 a more complex signal analysis is performed.

5.2.1 Non-resonant readout

The analysis of this configuration is very straightforward; since two simultaneous signal (i. e. signal and phase) are collected, it is possible to make a lock-in amplification. Assuming that no force is present in the tested range, this method will only reduce the background.
The two sets of data are processed from a software that follows the working principle of a lock-in amplifier: the normalized phase and the signal data are multiplied one to each other and then integrated with a low-pass filter. To have an output independent from the amplitude of the phase (since its value does not contain any information), it is normalized to a square wave going from 1 to -1, this tip permits to directly multiply signal and phase and proceed with integration. The low-pass filter integrates over frequencies above his cutoff frequency, so if a zero mean signal passes through the filter, it is gradually mediated to zero. Otherwise, if a signal in phase with the reference passed through the filter, it produces a DC current that is the output signal of the lock-in amplifier; instruments such as this allow to extract signals from a very noisy environment. Since the measured background is a the SQUID noise, whose origin is a thermal noise (as described in Section 2.3.2), it is a zero mean gaussian noise[2], that once is integrated reduces as $t^{-1/2}$, where t is the integration time [54].

To test code and algorithm a white gaussian noise was generated using the Marsenne-Twister generator [55] present in the boost libraries[3] and added to a known signal $\sin(\omega t)$, see Fig.(5.7).

[2] A method to confirm this is to verify is to collect multiple spectra and verify that the values of a single bin are distributed according to a gaussian curve.

[3] `http://www.boost.org/doc/libs/1_39_0/libs/random/random-generators.html`

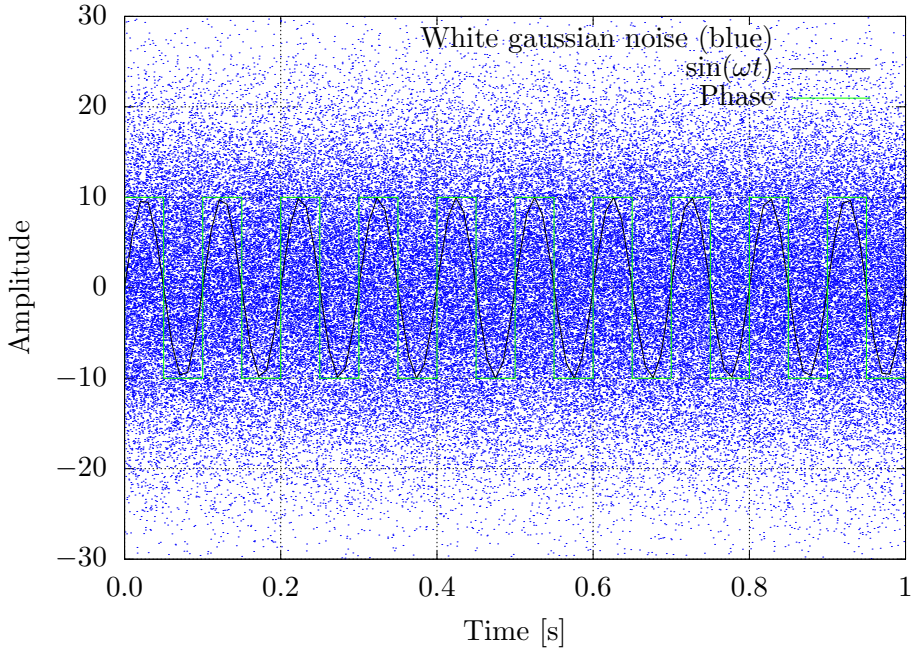

Figure 5.7: Test signal for the lock-in software, plotted together with a white gaussian noise generated randomly. The amplitude is in arbitrary units.

As previously explained, if the phase is normalized, a simple multiplication with the signal will provide for the mixer of the amplifier. Let $v_{\text{in}}(t)$ be the sequence $(v_{\text{in}}^1, v_{\text{in}}^2 \cdots v_{\text{in}}^n)$ and $v_{\text{out}}(t) = (v_{\text{out}}^1, v_{\text{out}}^2 \cdots v_{\text{out}}^n)$, the differential equation that describes the behavior of the filter is

$$v_{\text{in}}(t) - v_{\text{out}}(t) = RC\frac{\mathrm{d}v_{\text{out}}(t)}{\mathrm{d}t}, \tag{5.1}$$

where $\tau = RC$ is the time constant of the RC circuit. To simulate the low-pass filter, the discretization of Eq.(5.1) that rule the system yield

$$v_{\text{out}}^i = v_{\text{out}}^{i-1} + \frac{dt}{RC + dt}(v_{\text{in}}^i - v_{\text{out}}^{i-1}), \tag{5.2}$$

where dt is the time interval and v_{out}^i and v_{in}^i are the output and input signal i-th signals[4]. The test of this simple software is reported in Fig.(5.8), where it can be seen that the random background is reduced, while the presence of a signal with SNR$\sim$1 produces a DC signal.

[4]This configuration can be improved by means, for example, of a Butterworth filter.

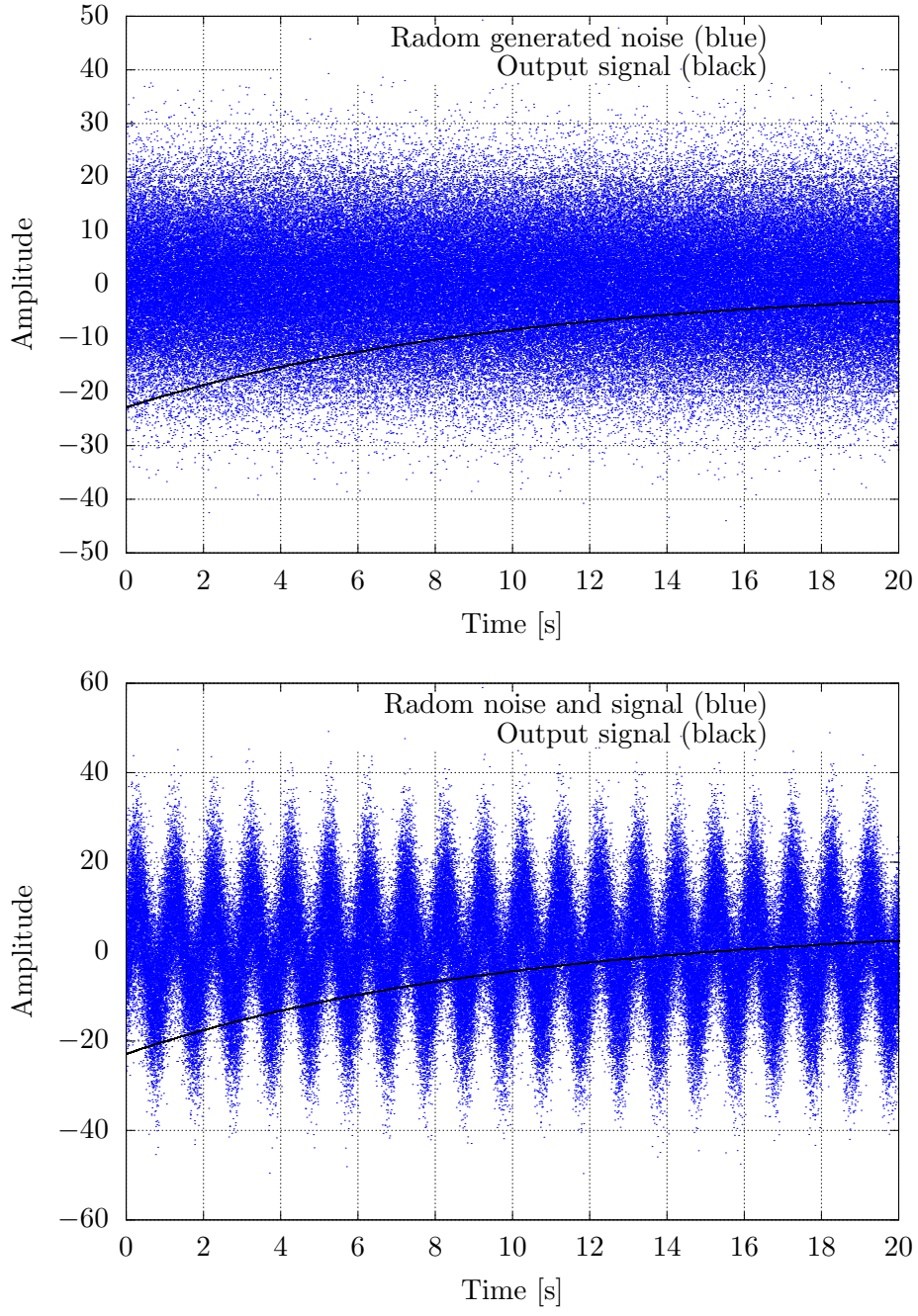

Figure 5.8: Output of the lock-in software for random generated noise and for noise and signal with SNR$\sim$1. The random noise produces a decreasing signal ($\rightarrow 0$), while the in-phase signal produce a DC signal (> 0).

The reference phase used for the test reported in Fig.(5.8) is a square wave that is positive when the sine is positive e negative if it is not, thus it is in-phase with the test signal as plotted in Fig.(5.7).

After this preliminary test it is possible to measure the output signal of the performed measurements, to obtain a limit of the measured field. The acquisition time t is 4 hours long, therefore it is expected to have a background reduction of a factor $\sqrt{t} \sim 120$, that, basing on spectrum in Fig.(5.4), predicts a background noise level of $\sim 1.6 \times 10^{-17}$ T. Considering now the integrated measurement reported in Fig.(5.6), the phase signal was normalized as described, and the whole acquisition was analyzed by the lock-in software. The output is reported in Fig.(5.9).

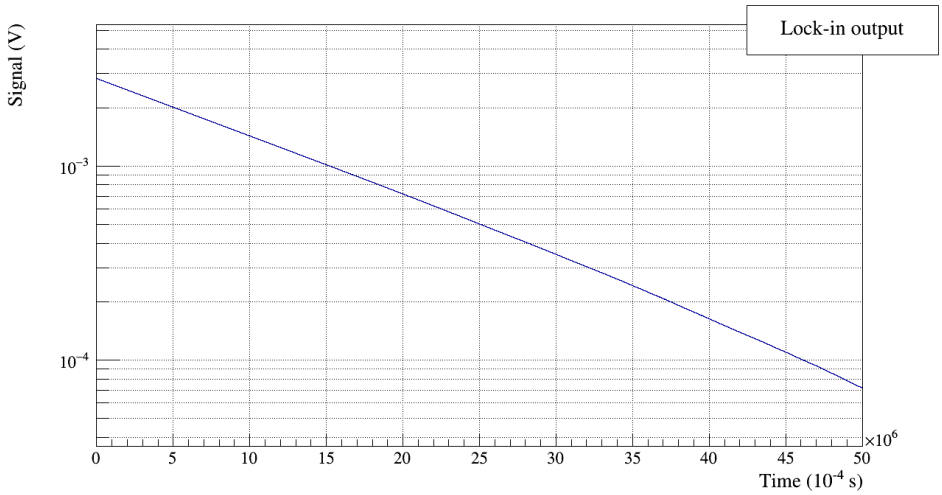

Figure 5.9: Decreasing output voltage of the lock-in. Note that the plot does not represent the whole acquisition.

A 4-hour long acquisition ($t = 15000\,\mathrm{s}$) integrated over time with the method described brought to a measure of a field $B_{\mathrm{eff}} = (0.34 \pm 0.51) \times 10^{-16}\,\mathrm{T}$. The error was calculated through a fit between experimental data and the $1/\sqrt{t}$ trend.

5.2.2 Resonant readout

In this section is performed an analysis of the expected spectrum given by the resonant circuit. In fact, differently from the non resonant configuration, the resonance will provide a spike in the spectrum due to the white noise lying

below the SQUID noise. The circuit used to simulate the readout is reported in Fig.(5.10), where the SQUID is substituted by a current generator (to make the function of noise) parallel to an amplifier.

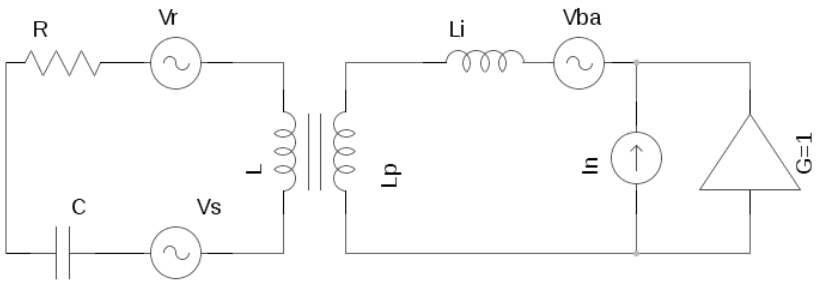

Figure 5.10: Circuit simulating the behaviour of the read out electronic and the SQUID. L, C and R are the inductance, capacity and resonance of the RLC circuit, respectively. V_r is the generator simulating the thermal (or magnetic) noise flowing in the circuit, while V_s is for the signal. L_p is the used pick-up coil, L_i is the internal coil of the SQUID, $V_{\rm ba}$ simulates the back-action of the SQUID and I_n represents its current noise.

To understand the behaviour of this circuit, working in the Laplace domain, one has to calculate the response function of the circuit, which is given by Eq.(5.3), where M is the mutual inductance between L and L_p, $M = k\sqrt{L_p L}$.

$$A(\omega) = \begin{pmatrix} i\omega\left(R - \frac{1}{i\omega C} + i\omega L\right) & -\omega^2 M \\ -\omega^2 M & -\omega^2(L_i + L_p) \end{pmatrix} \tag{5.3}$$

The transfer functions of the generators $S_{V_s} + S_{V_r}$ and S_{V_p} are reported in Eq.(5.4) and Eq.(5.5). V_p is the SQUID noise spectra. Usually $S_{V_p} = \epsilon L_i \omega^2$, where ϵ is the energy resolution of the SQUID and $S_{V_r} = 2Rk_BT$ is the noise (in the case of thermal noise):

$$T_s(\omega) = \begin{pmatrix} i\omega\left(R - \frac{1}{i\omega C} + i\omega L\right) & -\omega^2 M \\ i\omega & 0 \end{pmatrix}, \tag{5.4}$$

$$T_p(\omega) = \begin{pmatrix} i\omega\left(R - \frac{1}{i\omega C} + i\omega L\right) & -\omega^2 M \\ 0 & i\omega \end{pmatrix}. \tag{5.5}$$

To obtain the power spectrum read by the SQUID, which is the current flowing in the branch of I_n, the calculation yields

$$S_V^{\text{tot}}(\omega) = S_V^{(p)}(\omega) + S_V^{(s)}(\omega), \tag{5.6}$$

where the two components can be calculated from the transfer functions of Eq.(5.5) and Eq.(5.4):

$$\begin{aligned} S_V^{(p)}(\omega) &= V_p \frac{\det(T_p(\omega))\det\left(T_p^*(\omega)\right)}{|\det(A(\omega))|^2}, \\ S_V^{(s)}(\omega) &= (V_s + V_r)\frac{\det(T_s(\omega))\det(T_s^*(\omega))}{|\det(A(\omega))|^2}. \end{aligned} \tag{5.7}$$

Since the SQUID measures a current, the amplifier is basically a resistance, so if one supposes that $G = 1$, the gain of this amplifier, the current and the voltage have the same value. In this way the current noise I_n of the SQUID can be added to the power spectrum as $S_{I_n}(\omega) = 2\epsilon/L_{\text{SQUID}}$, where L_{SQUID} is the inductance of the loop.

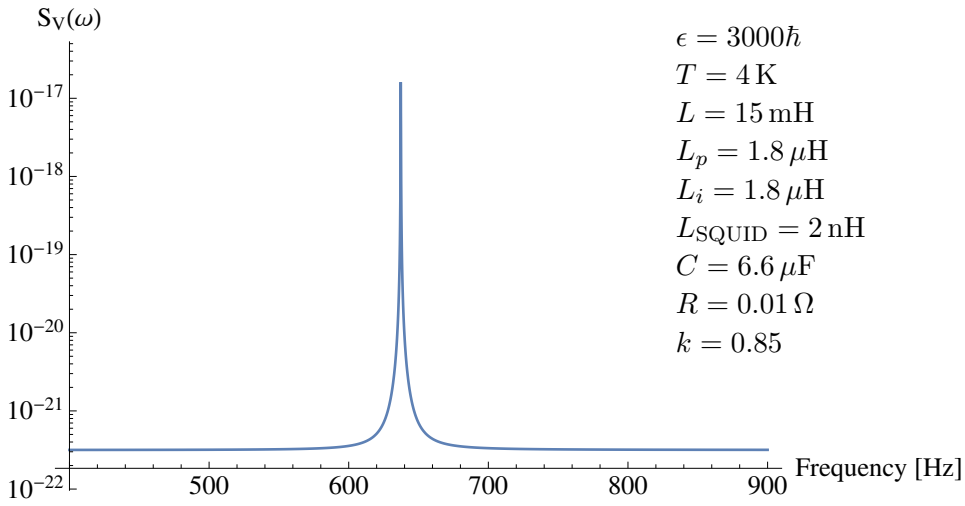

Figure 5.11: Computed spectrum of the measurement. The values used are reported on the right side of the figure.

Finally, the power spectrum that will be measured is given by Eq.(5.8) and are reported in Fig.(5.11).

$$S_V(\omega) = S_V^{\text{tot}}(\omega) + S_{I_n}(\omega). \tag{5.8}$$

Using the information of this spectrum and the experimental data, one can calculate precisely the losses of the circuit. A fit of this function with experimental data can provide unknown information about the apparatus, such as the contact and loss resistance R, or the mutual inductance coefficient k. A test of this analysis has been performed on the first data obtained with the SQUID resonant pick-up reported in Fig.(5.12).

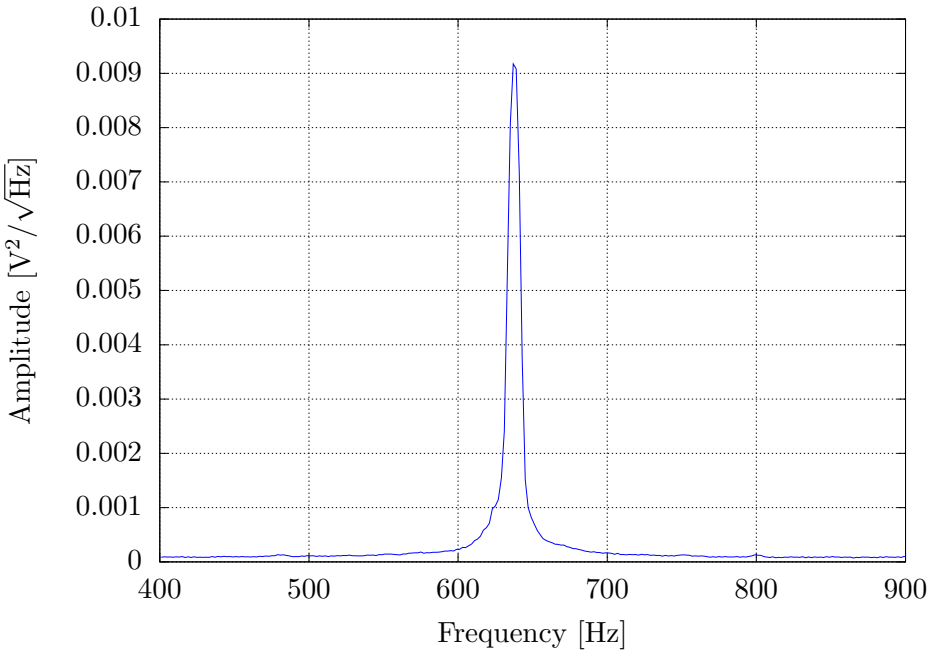

Figure 5.12: Preliminary data obtained with a resonant pick-up of the SQUID, the function in Fig.(5.11) is fitted over this experimental spectrum.

Clearly, some coefficients are implement to better evaluate the SQUID noise level and the scale between the two graphics. Using this procedure it is possible to verify the nominal ϵ of the SQUID, which is found to be correct as expected. The values obtained form the fit that were still unknown are

$$R = 0.23\,\Omega, \qquad k = 0.84.$$

This results, however, are not the final characteristics of the experiment. In fact the resonant pick-up is currently a work in progress, and test with different low-losses capacitor and coils are currently being performed. It can be noticed that Fig.(5.13) gives information also about the nature of

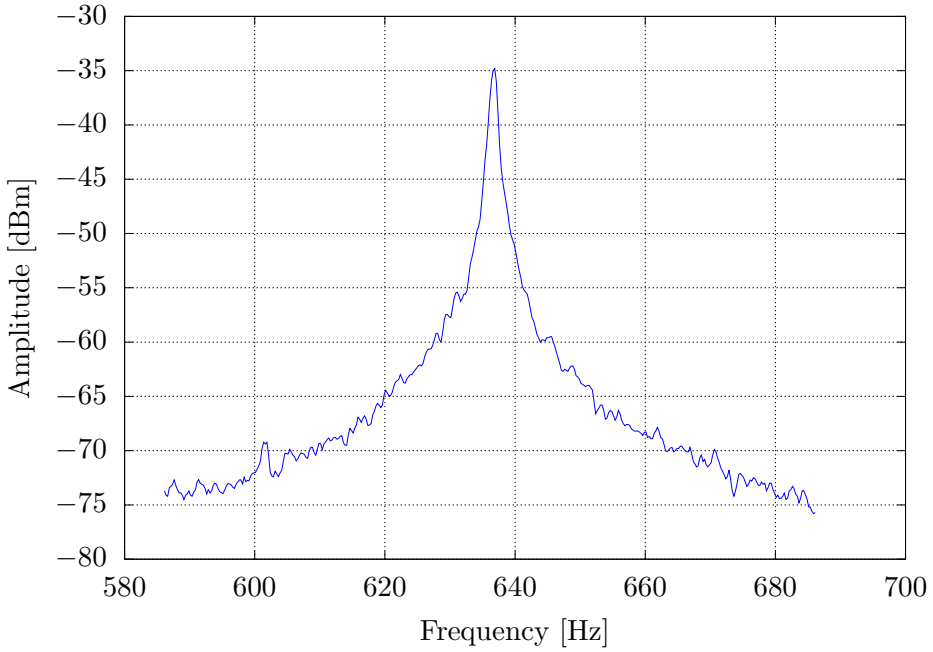

Figure 5.13: Preliminary data obtained with a resonant pick-up of the SQUID, detail of the resonance region.

the noise. The spike arises because of a white noise that is amplified by the resonance. Taking for example the case of pure white noise, the resulting spike turns out to be asymmetric. If another noise exists, which is above the white noise but not amplified by the resonance the lower part of the spike results covered by this noise, and, on first approximation will be symmetric. This is shown by the graphic produced in Fig.(5.11), where the covering noise is the one of the SQUID. Referring now to Fig.(5.13) and Fig.(5.12), it can be noticed that the spectrum is almost symmetric, this yields that the magnetization noise is (also in the resonant configuration) below the SQUID noise. This is expected, since another measure was performed to verify this fact, however, applying the same procedure to the thermal noise of the circuit, it is expected to be below the noise of the SQUID too.
Since the fit provided a value for the contact and losses resistance of the circuit, it is possible to estimate the Johnson-Nyquist noise of the circuit, given by the relation

$$S_V(\omega) = 4k_B T R. \tag{5.9}$$

Substituting the values of the apparatus in Eq.(5.9) one obtains

$$(S_V(\omega))^{1/2} = 7 \times 10^{-12}\,\mathrm{V}/\sqrt{\mathrm{Hz}} \rightarrow (S_B(\omega))^{1/2} = 3 \times 10^{-22}\,\mathrm{T}/\sqrt{\mathrm{Hz}}$$

which is less that the SQUID noise, as expected by the qualitative analysis. What results from a more detailed analysis, using the instruments already described in this section, is that that for a resistance $R \lesssim 1\,\Omega$ the thermal noise of the circuit is below the SQUID noise, therefore the gain of the SNR is equal to the Q factor of the circuit.
Since the tests on the resonant circuit are currently underway, no measured field will be reported but only a projection of the future sensitivity.

5.3 Results

As discussed, to give a limit on the coupling it is possible to detect an anomalous magnetization which comes from the effective field mediated by axions. The limit of this magnetization (i. e.) gives a limit on the axionic field, that can be reduced to an upper limit for the $g_p g_s$ coupling.

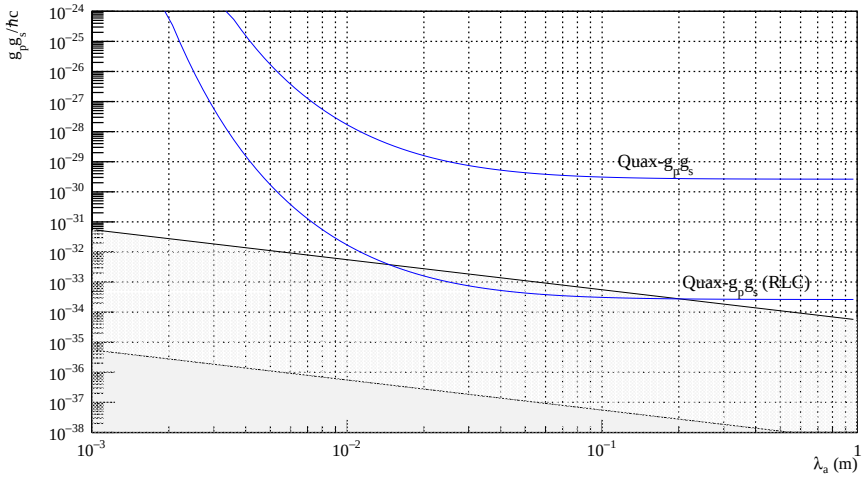

Figure 5.14: The gray-filled region represents the axion window discussed in Section 1.2.1 for $\theta = 10^{-10}$ (transparent color) and $\theta = 10^{-14}$ (solid color). The curve labelled as Quax-$g_p g_s$ is the limit already reached and measured. Quax-$g_p g_s$ (RLC) represent the limit that should be reached considering the background of Fig.(5.5) with the Q factor of the resonant circuit already obtained and reported in Fig.(5.13).

Using the Eq.(D.7) it is possible to obtain a plot showing the areas of the $g_p g_s/\lambda_a$ plane examined in this experiment. The plot in Fig.(5.14) shows the possible interaction region excluded by this measure and gives a projection of the imminent measure with the resonant configuration. Note that this values are compatible with what expected and reported in Fig.(5.12).
This establishes an upper limit of the combined values of mass (wavelength) and coupling of axions and ALPs, the final result is

$$B_{\text{eff}} = (0.34 \pm 0.51) \times 10^{-16}\,\text{T} \rightarrow g_p^e g_s^N \lesssim (2.7 \pm 4.0) \times 10^{-30},$$

for wavelengths of $\lambda_a \gtrsim 1\,\text{cm}$ as reported in Fig.(5.14), for $\lambda_a \lesssim 1\,\text{cm}$ the experiment loses sensitivity.

5.3.1 Possible limits on the $\bar{\theta}$ parameter

Referring to the graphic in Fig.(5.14), it is possible to deduce some more information about the physics involved. For example, assuming the presence of a mediator for this long-range ultraweak force, a limit on the $\bar{\theta}$ parameter can be given. Today's limit is $\bar{\theta} \lesssim 10^{-10}$ and is measured through an anomalous neutron electron dipole moment d_n, this experimental apparatus can be used also for testing the magnitude of this parameter to a similar order of magnitude or even to a smaller one. In fact, fixing the mass of the axion or ALP (or equivalently λ_a), it is possible to calculate the magnitude of the interaction, and therefore the value of $\bar{\theta}$. If the wavelength of the axion (or ALP) will result of the order of some cm, the resonant measure of this same experimental configuration will fix a constraint on $\bar{\theta}$ that is more accurate that the one derived from d_n.

Chapter 6

Conclusions

In this thesis is described a method to measure the $g_p^e g_s^N$ coupling with the QUAX-g$_p$g$_s$ experiment, the measurement reported fixes a new upper limit for this type of interaction.
At the beginning one can find a theoretical introduction which describes the specific physical phenomena and the main reasons to search for this interaction; placing some constraints on the measure it is possible to develop specific techniques to detect the considered effect. This leads to a description of the whole final set-up of the experiment, built during the thesis period, which consists in source, detector and read-out. Afterwards it is reported a specific study of the magnetic properties of the GSO crystal used in the experiment, that was completely characterized in terms of magnetic susceptibility and spin relaxation time using different experimental methods. With this information it is useful to make some tests of the background noise, from these first data an expected sensitivity of the experiment is determined, both at $\sim 10\,\mathrm{Hz}$ and $\sim 500\,\mathrm{Hz}$, that are the frequencies chosen for the measurement. Eventually are reported the definitive low-frequency measurements and the preliminary acquisition of the resonant configuration, with a detailed description of data analysis and results. Since the collected data confirm the expectations it is possible to conclude that this measures establish a new limit for the $g_p^e g_s^N$ interaction. In fact, considering an integration time of 4 h, the signal measured with the non resonant configuration is $B_{\mathrm{eff,min}} \simeq 10^{-17}\,\mathrm{T}$, with a resultant limit on the coupling $g_p^e g_s^N/\hbar c \lesssim 10^{-30}$ within $\lambda_a \gtrsim 1\,\mathrm{cm}$, that currently is the best limit measured for this spin-dependent force, as it is more accurate of one order of magnitude in respect of any previous measure.
Using a resonant circuit it is possible to improve this upper limit of 5 or-

ders of magnitude, reaching a magnetic field limit of $B_{\text{eff,min}} \simeq 10^{-22}$ T and therefore a coupling limit of $g_p^e g_s^N/\hbar c \lesssim 10^{-35}$.
A paper describing the apparatus has been currently submitted to *Nuclear Instruments and Methods*, the article titled "*The QUAX-$g_p g_s$ experiment to search for monopole-dipole Axion interaction*" is currently waiting to be published. Another article reporting the measurements of Section 5.2 is currently in course of writing.

6.1 Improvements

The ultimate aim of this type of experiments is to detect the presence of a force due to an axionic field, the models suggest that to do so it is necessary to reach the axion window reported in Fig.(5.14), therefore a higher precision is needed. In order to reach a higher sensitivity it is possible to use different expedients, some of them are briefly discussed in this section. Since QUAX-$g_p g_s$ is only sensible to monopole-dipole coupling, another improvement could be extend its possibility of measurement also to the dipole-dipole coupling, as proposed in Section 6.1.1. Some simpler improvements are discussed in Section 6.1.2, like use differential measurements to reduce the background or reduce the SQUID noise by improving the coupling k_i between the loop inductance L and the internal coil L_i. Finally, increasing the volume of the detector should produce a signal with a larger intensity. This can be done using a number of N_c crystals of GSO in series, read by the same SQUID with a resonant pick-up and is discussed in Section 6.1.3.

6.1.1 Polarized sources

A possible and interesting upgrade of this experiment is to make QUAX-$g_p g_s$ sensible also to the dipole-dipole interaction. This aim can be achieved by means of using a polarized source. In fact in the actual configuration only the detector (GSO crystal) is polarized, while the sources are not. This was already made by Adelberger *et al.* [36], the key feature that makes these torsion balance experiments sensitive to all the above interactions is the large macroscopic net intrinsic spin of the interacting masses. Different designs of test bodies have been developed aiming for a high density of polarized spins in masses from a few tens to a few hundreds of grams. The highest spin density achieved so far is about 3×10^{24} spins/kg obtained with a 29 g cylinder of Dy_6Fe_{23}. A slightly lower density of about 1.2×10^{24} spins/kg has been reached in with a 70 g composite structure of SmCo and AlNiCo.

These latter designs use ferromagnetic materials and permanent magnets due to the intrinsic alignment of a high number of electron spins. As a natural consequence, special attention in these designs has been given to suppressing magnetic effects. Magnetic shielding, magnetic compensation or magnetic field confinement have been exploited to ensure that the possibility of detecting any potential spin interaction is not limited by magnetically induced systematic errors.

A work by Carbone *et al.* [59] presents conceptually new designs for spin-polarized masses based on permanent magnets. The idea of a concentric assembly of permanent magnets comes from the need to neutralize the magnetic field produced by pairs of counter-aligned permanent magnets, while retaining their individual magnetic properties. Although this may seem difficult to realize because of the impossibility of the physical superposition of two magnetic moments, the use of simple geometries makes this feasible, as reported in Fig.(6.1).

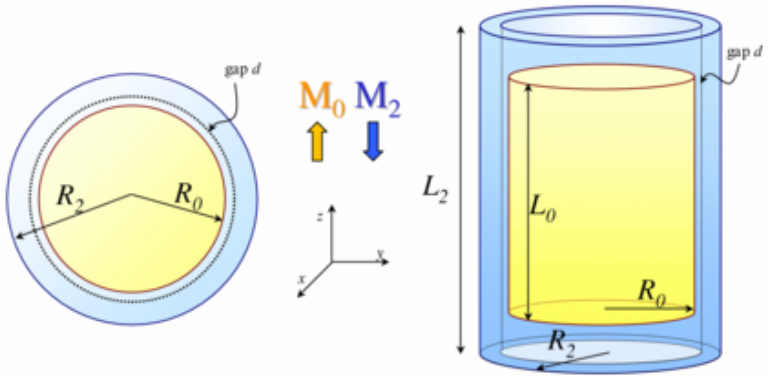

Figure 6.1: Left: nested arrangement of a uniformly magnetized sphere within a spherical shell. Right: nested arrangement of two cylinders [59]. Subscript 0 relates to the inner magnet while 2 is for the outer one.

Designing a concentric assembly of permanent magnets whose relevant m lm moments are equal and opposite still nominally allows the minimization, or even the nulling, of the magnetic behavior of the system.
The use of this kind of samples make it possible to detect a dipole-dipole interaction, since both the source and detector are polarized, and limits the disturbing magnetic effects introduced by the masses, allowing to measure a limit for this interaction too. Using this technique, instantaneous noises coming form the environment are read both from both the sources, so no signal is measured.

6.1.2 Differential measurement

The first spectra gathered during the tests, referring to Fig.(4.3), shows that the background is somewhere afflicted by vibrational noise peaks. As discussed, the SQUID sensitivity is such that also acoustic vibrations present in the measure environment disturbs the acquisition. To damp this effect it is possible to perform a differential measurement, as to compare to crystal in the exact same condition, of which one is affected by the interaction while the other does not, according to the scheme in Fig.(6.2). Using this technique, instantaneous noises coming form the environment are read from both the sources, so no signal is measured.

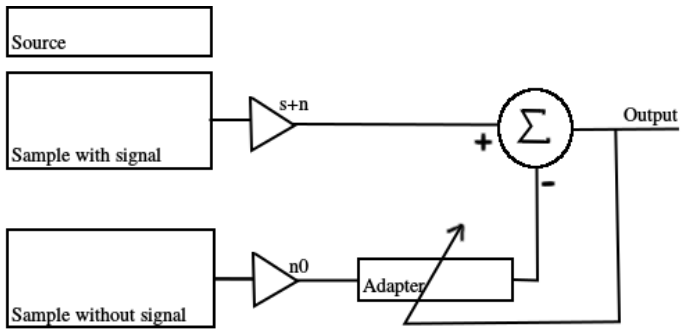

Figure 6.2: Scheme of the differential measure with two detectors. $s + n$ represents the signal and noise coming from the first sample, while n_0 represents the noise coming from the second one, which is not affected by the interaction.

The problem of this configuration is letting the interaction affect only one sample, since the two has to be very close, as to measure the same noises. A possible solution that can be exploited is to use the same detector providing both for the sample biased by the signal and for the other. This could be possible taking advantage of the geometry of the experiment. Considering that the interaction acts only on the direction $\hat{\boldsymbol{r}}$, another pick-up coil wrapped on the same crystal with the axis perpendicular to $\hat{\boldsymbol{r}}$ should stand for the background sample, as it is not affected by the interaction. This can be a useful tool, but need some test, since its working principle suppose that the noises, differently from the signal, is isotropic. Such thing is not verified in principle and could produce errors in the measurement. Note that this analysis can also be done a posteriori, taking two measures, with and with-

out sources. This will lead to the same result only if the exact external noise are present during the two acquisition, but since the main sources of disturb to be removed are environmental this condition is not always satisfied.
Another way to directly improve the measure is to use a SQUID with a better coupling between the internal coil L_i and the inductance of the loop L, i. e. to have a higher value of k_i. Since such SQUIDs are commercially available, so the noise of the magnetometer will result improved dependently on the coupling k_i. As a consequence, the internal coils L_i of this devices, typically have inductances of the order of some nH, therefore a suitable pick-up of the signal has to be developed.

6.1.3 Superconducting transformer

Consider the simple measuring scheme of Fig.(2.12) in which the coupling between the GSO sample and the dc-SQUID is done by means of a superconducting transformer composed by the pick-up inductance L_p wound on the GSO and the SQUID input coil L_i coupled to the SQUID loop L_l by means of the mutual inductance M_i. In this scheme, the noise sources that can be modeled are the SQUID noise and the thermal noise due to the magnetic losses of the GSO crystal. As regards the SQUID, in this case, as for the majority of applications at audio frequencies without high Q resonating input load [56], its noise can be modeled as an additive flux noise at the SQUID loop with power spectral density S_ϕ or its equivalent energy resolution $\epsilon = S_\phi/(2L_l)$. It is easy to show (see Section 2.3.1 [41]) that the equivalent noise energy referred to the pickup loop ϵ_p can be minimized when $L_p = L_i$ and its optimal value is $e_p = (4/k_i^2)\epsilon$. By operating with this optimal coupling and approximating the L_p inductance to that of a long solenoid of volume V, one can show that the equivalent magnetic field noise applied to the pick-up is given by $S_B^{1/2} = (2/k_i)(2\mu\epsilon/V)^{1/2}$ where mu is the permeability of the GSO crystal and V its volume. As an example, consider a cylindrical GSO sample ($\mu \simeq 1.7$), 30 mm in diameter and 200 mm in height, with 20 turns of pick-up. Its expected inductance is about 1.7 μH, a value near the typical input inductance of some commercial SQUIDs. In the best case one can consider a SQUID with an energy resolution of $1\hbar$, an ideal quantum limited SQUID, with a coupling constant $k_i = 1$. In this case the expected equivalent magnetic field noise applied to the pick-up is $3.9 \times 10^{-18}\mathrm{T}/\sqrt{\mathrm{Hz}}$. The noise source associated to the paramagnetic GSO crystal depends on the imaginary component of its magnetic susceptibility (see Chapter 3). In particular, the resistive component of the pick-up inductance wound on the GSO is given by $\omega^2 L_p' \chi_0 \tau_M$ where ω is the angular

frequency, $L'_p = \mu L_p$, χ is the magnetic susceptibility, and τ_M is the spin relaxation time. In this case, it can be shown that, at the audio frequencies of interest, the equivalent magnetic field noise at the pick-up is given by $S_B^{1/2} = 2(2\mu(k_B T \chi_0 \tau_M)/8V)^{1/2}$. This noise, at 4 K and with the values of χ_0 and τ_M reported in Chapter 3, becomes comparable to the noise due to the SQUID only if the latter operates at the quantum limit.

Other possible schemes can improve the signal-to-noise ratio. Here will briefly mentioned a few variants of the basic scheme of figure 2.12. From Eq.(4.1) for the equivalent magnetic field noise at the pick-up one can infer that this can be reduced a twill by simply increasing the volume of the GSO crystal. This is possible only as long as the inductance of the coil wound on the crystal can be kept approximately equal to the input coil inductance of the SQUID which is typically less than 2 μH. To overcome this limit one can use a superconducting low-losses matching transformer [57] that permits to optimally couple pick-up coils with inductance of the order of 1-10 H to the SQUID input coil. The typical dimensions of the paramagnetic crystal and, as a consequence, of the rotating mass that constitutes the signal source, are determined, as well as by practical constraints, by the range of the values of parameter λ_a it is intended to test. To keep the crystal dimensions of the order of 1 cm but to reduce the equivalent magnetic field noise at the pick-up due to the SQUID, it is convenient to use a number N_c of crystals with their pick-up coil connected in series. In this case, Eq.(4.1) is still valid if V represents the total volume of the N_c crystals. Of course, also the number of the rotating masses has to be equal to N_c in order to generate signals in phase in the N_c pick-up coils of the crystals connected in series. Compared to the SNR of the single crystal optimally coupled to the SQUID this configuration would permit an improvement of a factor N_c^2.

Another strategy to improve the signal-to-noise ratio consists in using a resonating matching circuit. If a low-losses capacitor is connected in series to the primary coil of the matching transformer and the N_c pick-up coils, so that the circuit resonates at the frequency of the signal, it is easy to demonstrate that the flux signal at the SQUID is increased by Q, the quality factor of the resonant circuit. In order to quantify this improvement, observing that, if the losses of the resonant circuit operating at, let's say, 500 Hz were entirely due to the GSO crystal, according to the values of χ and τ_M given in Section 3, the circuit quality factor could be of the order of 10^6. This means that the GSO magnetic losses are negligible compared to the intrinsic losses of this type of LC resonators that can achieve quality factors of the order of 10^6 [58].

Acknowledgments

This work of thesis involved a lot of people, from the beginning to the end of this experience I always found someone willing to teach and help me, and I am grateful for this.
I would like to thank Mario Tessaro, Fulvio Calaon and Enrico Berto for all the help with the building of the apparatus and with the measurement, Giuseppe Galeazzi for his willingness and for the patience he had while sharing with me his great experience and Professor Paolo Falferi, who introduced and guided me in the use of the SQUID. I also thank Professor Clive Speake, for the useful discussion about the dipole-dipole coupling and the $\bar{\theta}$ parameter and Professor Paride Paradisi for the precise suggestions and useful advice regarding the theoretical part of the work.
Of course my gratitude goes to the extraordinary group I worked with: Antonello Ortolan, Giuseppe Ruoso and Caterina Braggio, who have such a deep understanding of physics. Above all I would like to thank Professor Giovanni Carugno for sharing with me his deep knowledge about physics and the incomparable passion for his work.

Appendix A

Axionic couplings

The possible interaction between mediated by a scalar particle are given by three vertexes, which combined gives the three different couplings, *monopole-monopole*, *monopole-dipole* and *dipole-dipole*, reported in Fig(A.1). The first is spin-independent, while the other two are not, in particular the *dipole*^{2} depends only on the spin.

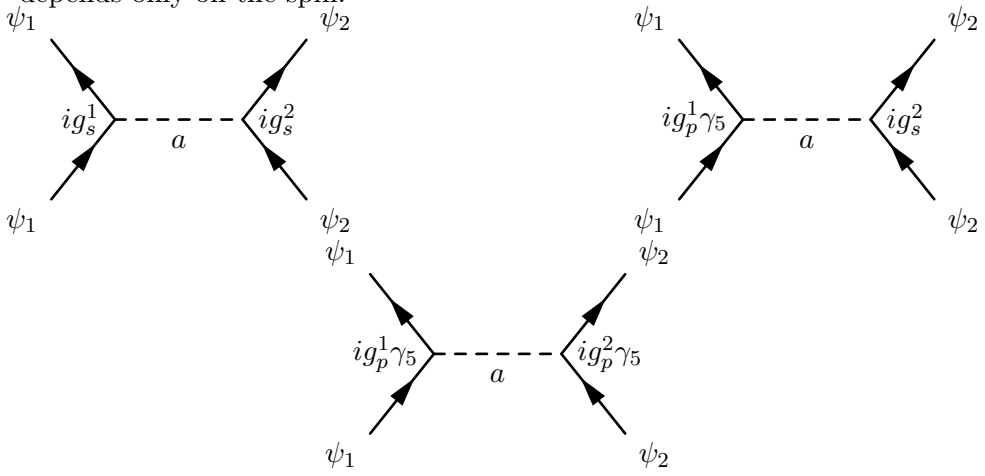

Figure A.1: Interaction diagram of all spin-0 boson couplings between two fermions ψ_1 and ψ_2. The scalar vertex has the coupling constant g_s, whereas the pseudoscalar vertex has g_p. The mediator is the axion a and the interaction strength is proportional to $g_s g_p$, $g_p g_p$ or $g_s g_s$.

Starting from Eq.(1.14) one can calculate the potential for the three macroscopic forces which arises between the fermons.

A.1 Monopole-monopole

For the *monopole-monopole* coupling one obtains the potential of Eq.(A.1)

$$V_{mm}(\boldsymbol{r}) = -\frac{g_s^1 g_s^2 e^{-\frac{r}{\lambda_a}}}{4\pi r}, \tag{A.1}$$

his coupling constant value can be calculated [25], and results

$$g_s g_s = \Big(\frac{\theta\sigma}{f_a}\frac{2m_u m_d}{(m_u+m_d)^2}\Big)^2, \tag{A.2}$$

where all the symbols used has been already defined in Section 1.2.1.

A.2 Monopole-dipole

In the case of the *monopole-dipole* coupling, which has been considered in Section 1.2, the calculation yields

$$V_{md}(\boldsymbol{r}) = \frac{g_p^1 g_s^2}{8\pi m_1}\Big[(\hat{\boldsymbol{\sigma}}\cdot\hat{\boldsymbol{r}})\Big(\frac{1}{r\lambda_a}+\frac{1}{r^2}\Big)\Big]e^{-\frac{r}{\lambda_a}}. \tag{A.3}$$

For further discussion of this interaction see Section 1.2.

A.3 Dipole-dipole

As can be seen in Fig.(A.1), there is another coupling permitted for electronic spin, which is the $(dipole)^2$. For this interaction the potential is given by Eq.(A.4),

$$V_{dd}(\boldsymbol{r}) = \frac{g_p^1 g_p^2}{16\pi m_1 m_2 r^3}\Big[(\hat{\boldsymbol{\sigma_1}}\cdot\hat{\boldsymbol{\sigma_2}})\Big(1+\frac{r}{\lambda_a}\Big)-3(\hat{\boldsymbol{\sigma_1}}\cdot\hat{\boldsymbol{r}})(\hat{\boldsymbol{\sigma_2}}\cdot\hat{\boldsymbol{r}})\Big(1+\frac{r}{\lambda_a}+\frac{r^2}{3\lambda_a^2}\Big)\Big]e^{-\frac{r}{\lambda_a}}. \tag{A.4}$$

Like the other one, for a macroscopic body this can be interpreted as an effective magnetic field, the consideration reported in Section 1.2 are true for this field too. The value of the the coupling constant is

$$g_p^2 = \Big(\frac{m_a}{f_a}\Big)^2, \tag{A.5}$$

a comparison between the intensity of the *monopole-dipole* and *dipole-dipole* interaction is shown in Fig.(1.3). Their relative intensity depends heavily on the λ considered.

Appendix B

Resonant circuits

There are several possibilities for the design of the resonant circuit, two of them are reported in Fig.(B.1).

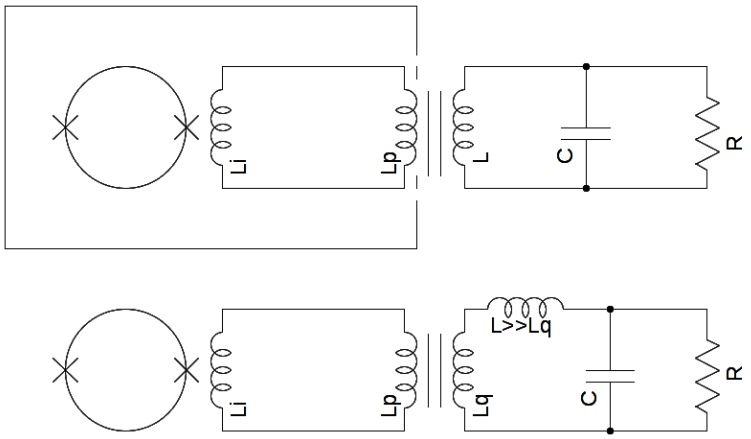

Figure B.1: Possible designs of the resonant circuits, coupled with the SQUID. The resistance R is an equivalent resistance (superconduction regime), L_i is the internal inductance of the SQUID, and L_p is the pick-up coil.

Here will be performed brief analysis of the two circuits above, considering initially the signal given by the simple circuit in the black square, with $L_p \simeq L_i$. If B is the signal of the axionic field, a is the section and n the

number of spires of the pick-up coil, one can write,

$$\delta\phi_i + (L_i + L_p)I_i = (an)\,B + 2L_pI_i = 0. \tag{B.1}$$

So the interested signal can be measured through the relation:

$$I_1 = -\frac{(an)\,B}{2L_p}. \tag{B.2}$$

Now, considering the whole circuit in figure, and supposing the flux to be collected only by the solenoid L (which has his own section A and number of spires N), the coupling is $M = k\sqrt{L_pL}$. At the resonant frequency of the circuit, considering $k = 1$, the signal is given by:

$$I_2 = \frac{AN\,B}{\sqrt{L_pL}}Q, \tag{B.3}$$

so the gain, compared with the one of the previous configuration, if $a = A$, is

$$\begin{aligned}\frac{|I_2|}{|I_1|} =& \frac{AN\,B}{\sqrt{L_pL}}\frac{2L_p}{an\,B} = 2\frac{N\,B}{\sqrt{L_pL}}\frac{L_p}{n\,B}\\ =& 2\frac{L_p}{\sqrt{L_pL}}\sqrt{\frac{L}{L_p}}Q = 2Q.\end{aligned} \tag{B.4}$$

Another configuration can be given by the second circuit in figure, where the hypothesis is that the field B is collected entirely by L. This biggest solenoid have $L \gg L_p$ (with $L_p = L_q$), and, since $L_i = L_p$ one obtains $M = L_p$, and equations like the ones used before, with signal I_3 yields:

$$\begin{aligned}\frac{|I_3|}{|I_1|} =& \frac{AN\,B}{2L}\frac{2L_p}{an\,B} = Q\frac{AN}{an}\frac{L_p}{L}\\ =& \frac{AN}{an}\frac{n^2a}{N^2A}Q = \frac{n}{N}Q\end{aligned} \tag{B.5}$$

The noise produced by this circuits is different, and has to be taken into account; for the simplest circuit the noise is calculated in Appendix 2.3.2. For the other two circuits the main source of noise is the Johnson's noise of the resistor, so the relation to be respected, if the spectral density of the noise is $S^{2,3}$ (given by $I_{2,3}$) and ω is the frequency, is

$$S^{2,3}_\phi(\omega) > \frac{4k_bTR}{\omega^2} \quad \rightarrow \quad S^{2,3}_B(\omega) > \frac{4k_bTR}{S^2N^2\omega^2}. \tag{B.6}$$

Considering a resistance $R \simeq 0.01\,\Omega$ at a frequency of 600 Hz and the actual pick-up coil, the resulting magnetic field noise is $S^{2,3}_B(\omega) = 2.0{\cdot}10^{-24}\,\mathrm{T}/\sqrt{\mathrm{Hz}}$.

Appendix C

YIG magnetization noise

The magnetization noise was measured with a SQUID based magnetometer and from this measurement the imaginary part of the magnetic susceptibility can be estimated. The noise spectrum has an intensity $\sqrt{S_B(\omega)} \simeq 40\,\mathrm{fT}/\sqrt{\mathrm{Hz}}$ in the frequency range from 1 kHz to 100 kHz, from this measurement, after a fit with the equation given by the fluctuation-dissipation theorem, was obtained the imaginary part of the susceptibility $\chi'' \simeq 0.002$. Since the sample has a spherical shape, a geometric normalization is needed, these factors were calculated from a numerical simulation.

C.1 Introduction

Yttrium Iron Garnet (YIG) is a ferrimagnetic material belonging to the rare-earth garnets with a chemical formula $Y_3Fe_2(FeO_4)_3$. It has interesting magnetic properties such as high density of unpaired electron spin, low dissipation of magnetization and a sharp resonance at the Larmor frequency tunable with a static magnetic field.
In this kind of materials the magnetism is determined by the electron spin, they are moved by the thermal bath and this generates a noise in the entire magnetization of the dissipative sample in accordance with the fluctuation dissipation theorem. The magnetic noise is related to the imaginary part of susceptibility of the material, in fact, when a sample is placed inside an inductance, a resistivity term arises and it is a source of Johnson-Nyquist noise.
In this studies was measured the magnetic noise of a spherical sample of crystalline YIG at 4.2 K using a magnetometer based on a dc-SQUID.

C.2 Experimental setup

The pickup loop is connected to a Magnicon dc-SQUID C6XXL1W with a niobium cable of negligible inductance (see figure C.1), the condition that minimize the noise referred to the pickup loop is $L_{\mathrm{p}} = L_{\mathrm{in}}$. The magnetometer is mounted on a stainless steel bar which is the connection between the warm and cold phases of the experiment. The set-up is placed inside a dewar filled of liquid helium-4. The YIG sample is a sphere of radius 1 mm and it is coupled with a 24 turns pickup loop made out of superconductive niobium wires. The pickup loop has 6 mm of length and 1.5 mm of radius, the 24 turns are divided symmetrically in two group with an internal gap of 2.8 mm. This configuration forces to consider some geometrical and coupling factors in order to correct the theoretical result, which will be calculated in the next section.

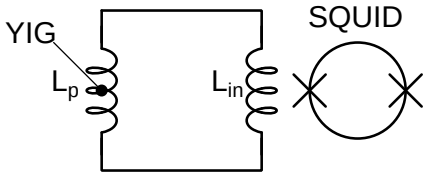

Figure C.1: Magnetometer circuit with YIG sphere inserted in the pickup loop.

The magnetometer is immersed in glycerin for mechanical noise suppression and a cylindrical superconductive lead shield is applied for electromagnetic noise control. The calibration system is realized by a large cylindrical solenoid mounted coaxially to the pickup loop, in which is induced a small current at different amplitudes and frequencies. A Hewlett-Packard 35660A spectrum analyzer is used to process and collect the data. The reported noise of the SQUID is $S_\phi(\omega) \simeq 1\,\mu\phi_0/\sqrt{\mathrm{Hz}}$ for frequencies above 1 kHz, the corner frequency of the $1/f$ noise is around 0.1 Hz. The magnetometer exhibits a measured noise of $\sqrt{S_B(\omega)} \simeq 6 \times 10^{-15}\,\mathrm{T}/\sqrt{\mathrm{Hz}}$ in the considered frequency range, this value is taken as the sensitivity of this instrument. The temperature was controlled through a Pt100 thermometer placed inside the superconductive shield.

After the optimization of the transfer function of the SQUID the system is calibrated with a known magnetic field, in this way is verified the linearity in frequency and amplitude of the magnetometer. Then it is possible to collect a spectrum of the YIG magnetic noise over a range of frequency from 1 kHz to 102 kHz.

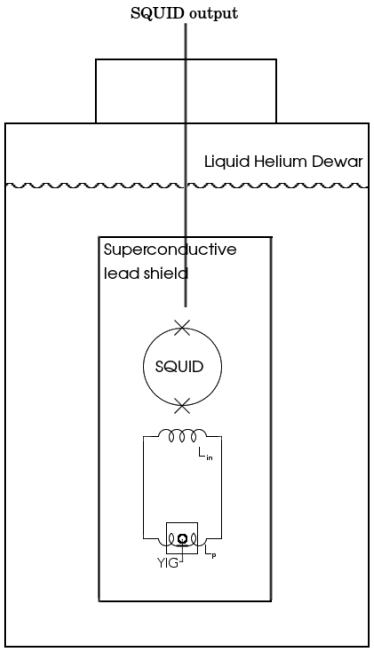

Figure C.2: Scheme of the apparatus.

C.3 Measurement result

Viscosity term of pickup loop partially filled with YIG is $R_s = 4\pi\xi L_p \chi''(\omega)$, where $\xi = V_{\text{YIG}}/V_{\text{coil}}$ is the fraction of occupied volume and L_p is the inductance of empty pickup loop. R_s is a source of voltage noise with a spectral density $S_V(\omega) = 4k_B T R_s$, the related magnetization noise that produce this voltage fluctuation is

$$S_B(\omega) = C\frac{k_B T \chi''(\omega)}{\omega}, \tag{C.1}$$

where C is a constant that contains ξ and circuit's components reported in Fig.(C.1), the calculation yields $C = \frac{16\pi\xi L_p^3}{N^2 A^2 \zeta (L_p + L_{in})^2}$, where ζ is a geometrical factor that take into account the coupling between the YIG sphere and pickup inductance. To estimate the effective flux collected by the pickup coils (e.g. ζ), a simulation of the internal field of a spherical YIG was carried out. The measured current is due to a fraction of this magnetization noise, that can be estimated with $\zeta = \phi_{\text{coil}}/\phi_{\text{eff}}$.

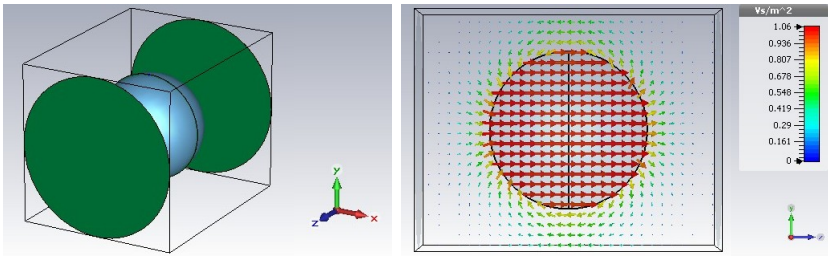

Figure C.3: Perspective of the configuration of the pickup coils and resulting field from the simulation of the coupling. The left figure represents the YIG sphere (grey) and the pickup coil area (green), while the right figure represents the vectors of the magnetization field on the symmetry plane of the coil.

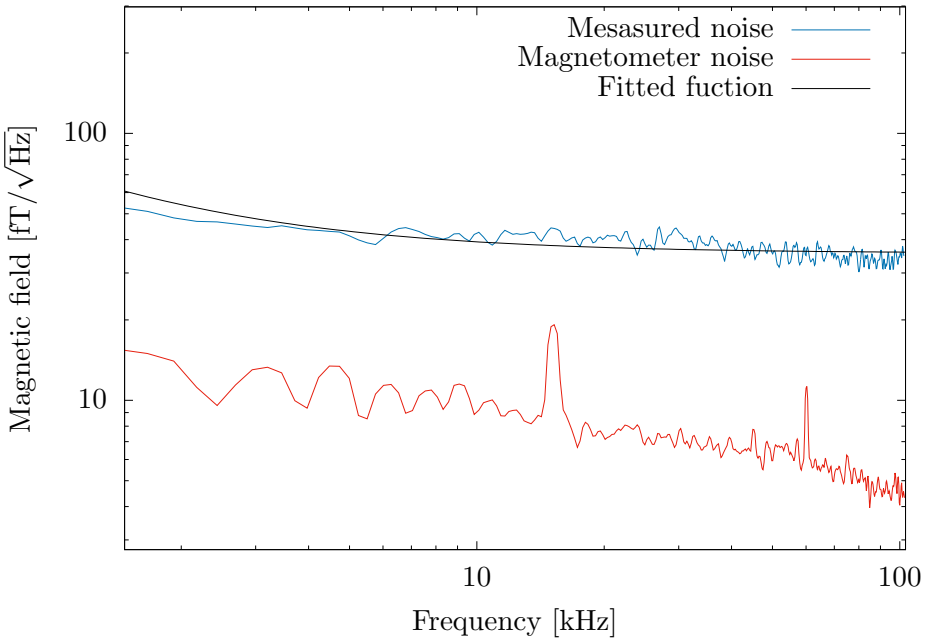

Figure C.4: Spectrum of the measured magnetization noise (blue) and spectrum of the magnetometer's noise (red). In black is reported the fitted function of the Johnson-Nyquist noise, used to estimate χ''.

This simulation permits to calculate the value of the constant $C \simeq 0.19\, Hm^{-4}$.

The measured magnetization noise, together with the intrinsic noise spectrum of the magnetometer, is reported in Fig.(C.4).
As can be seen, the measured noise is considerably above the sensitivity of the magnetometer, and respects the prediction of the fluctuation dissipation theorem (black continuous line in Fig.(C.4)). The results of the fit gives $\sqrt{C \cdot k_B T \chi''} = 27 \pm 1\,\mathrm{fT}$, that yield an imaginary part of the susceptibility $\chi'' = (1.1 \pm 0.1) \times 10^{-4}$

C.4 Conclusions

Considering the results reported in the previous section (C.3) and in Chapter 4, it is clear that the magnetization noise of the YIG does not permit a higher SNR, even if the magnetic susceptibility $\chi_0^{\mathrm{YIG}} > \chi_0^{\mathrm{GSO}}$. Other works [35] also suggest that in this case, the domain wall noise limits the sensitivity even more than the magnetization noise. It is therefore clear that the GSO will provide a better detector that the YIG for the measurements of the QUAX-$g_p g_s$ experiment.

Appendix D

Integration of the effective field

The potential caused by a *monopole-dipole* coupling between an unpolarized nucleon and a polarized electron with mass m and spin σ is given as function of the interaction range λ_a as [25]

$$V_{md}(\boldsymbol{r}) = \frac{\hbar g_p^e g_s^N}{8\pi m_e c}\Big[(\hat{\boldsymbol{\sigma}}\cdot\hat{\boldsymbol{r}})\Big(\frac{1}{r\lambda_a}+\frac{1}{r^2}\Big)\Big]e^{-\frac{r}{\lambda_a}}, \tag{D.1}$$

where $\hat{\boldsymbol{r}}$ is the unit vector of the position

$$r = (\phi, t, z') \tag{D.2}$$

in cylindrical coordinates between the electron and a nucleon. In order to evaluate the total potential $V_{\mathrm{tot(z)}}$ of many nucleons within bulk matter, e.g. an infinite plate of thickness d, as function of the height z of the electron above the matter surface, the frame of reference in Fig.(D.1) is considered. For obtaining $V_{\mathrm{tot}}(z)$, it is necessary to integrate over all possible nucleon coordinates:

$$V_{\mathrm{tot}}(z) = \int_0^{-d}\int_0^{+\infty}\int_0^{2\pi} nV_{md}(\boldsymbol{r})\, d\phi\, t dt\, dz', \tag{D.3}$$

where n is the nucleon density of the bulk matter plate which is located with its upper surface at $z' = 0$ and its lower surface at $z' = -d$. Only cases with neutron spin σ normal to the surface are taken into account. Thus the scalar product $\sigma\cdot\hat{\boldsymbol{r}}$ in Eq.(D.1) can be evaluated by using the vector $-\sigma$ as sketched in Fig.(D.1):

$$-\sigma\cdot\hat{\boldsymbol{r}} = \cos(\theta) = \frac{z^*}{\sqrt{z^{*2}+t^2}}, \tag{D.4}$$

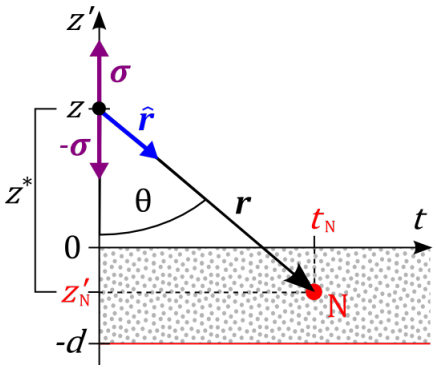

Figure D.1: Sketch of the frame of reference to derive a pseudomagnetic field caused by a short-range spin dependent interaction [60]. The radial coordinate t is given on the abscissa and the vertical coordinate z' is given on the ordinate. Bulk matter in form of a plate of thickness d and infinite radius is depicted by grey dots. An exemplary nucleon N is depicted as red circle and its coordinates are subscribed with N. The electron is depicted by a black circle and its spin vector σ by a purple arrow.

where $z^* \equiv z - z'$, and $z' < 0$ and t are the coordinates of the nucleon N in the sketch. The length of the position vector r is given by

$$r = |r| = \sqrt{z^{*2} + t^2}. \tag{D.5}$$

Using Eq.(D.3), Eq.(D.5) can be evaluated as

$$\begin{aligned}
V_{\text{tot}}(z) &= \frac{\hbar g_p^e g_s^N}{8\pi m_e c} n \int_0^{-d}\int_0^{+\infty}\int_0^{2\pi} \Big[\cos(\theta)\Big(\frac{1}{r\lambda_a} + \frac{1}{r^2}\Big)\Big] e^{-\frac{r}{\lambda_a}}\, d\phi\, t dt\, dz' \\
&= \frac{\hbar g_p^e g_s^N}{4m_e c} n \int_0^{-d}\int_0^{+\infty} \Big[\frac{z^*}{\sqrt{z^{*2}+t^2}}\Big(\frac{1}{\sqrt{z^{*2}+t^2}\lambda_a} + \frac{1}{z^{*2}+t^2}\Big)\Big] e^{-\frac{\sqrt{z^{*2}+t^2}}{\lambda_a}}\, d\phi\, t dt\, dz' \\
&= \frac{\hbar g_p^e g_s^N}{4m_e c} n \int_0^{-d} -e^{-\frac{z^*}{\lambda_a}}\, dz' = \frac{\hbar g_p^e g_s^N}{4m_e c} n \int_0^{-d} -e^{-\frac{z-z'}{\lambda_a}}\, dz' \\
&= \frac{\hbar g_p^e g_s^N}{4m_e c} n\lambda_a \Big(- e^{-\frac{z+d}{\lambda_a}} + e^{-\frac{z}{\lambda_a}}\Big) = \frac{\hbar g_p^e g_s^N}{4m_e c} n\lambda_a (1 - e^{-\frac{d}{\lambda_a}}) e^{-\frac{z}{\lambda_a}}
\end{aligned} \tag{D.6}$$

where the integral over dt was solved using Wolfram Mathematica, and z^* was resubstituted by $z - z'$ [60].

It is possible to solve the integral also for a finite region of space (i.e. the surface of the sources). The detailed derivation is omitted, since it can be done with a calculation tool (Mathematica). Adding the parameter t standing for the surface radius of the source, one obtains

$$V_{\mathrm{tot}}(z) = \frac{\hbar g_p^e g_s^N}{4 m_e c} n \lambda_a \left(e^{-\frac{\sqrt{(t+z)^2+\mathrm{d}^2}}{\lambda}_a} - e^{-\frac{z+t}{\lambda}_a} - e^{-\frac{\sqrt{d^2+z^2}}{\lambda}_a} + e^{-\frac{z}{\lambda_a}} \right). \tag{D.7}$$

This is the most precise estimation of the total field acting on the detector, which is still considered as a point, and will therefore be the formula used to estimate the actual signal. It is to be noticed that the differences between Eq.(D.7) and Eq.(D.6) are hardly appreciable for the considered scales.

Bibliography

[1] S. Weinberg, "Approximate symmetries and pseudo-goldstone bosons," *Phys. Rev. Lett.*, vol. 29, pp. 1698–1701, Dec 1972.

[2] R. D. Peccei and H. R. Quinn, "CP conservation in the presence of pseudoparticles," *Phys. Rev. Lett.*, vol. 38, pp. 1440–1443, Jun 1977.

[3] R. D. Peccei, *The Strong CP Problem and Axions*, pp. 3–17. Berlin, Heidelberg: Springer Berlin Heidelberg, 2008.

[4] S. Weinberg, "The u(1) problem," *Phys. Rev. D*, vol. 11, pp. 3583–3593, Jun 1975.

[5] G. 't Hooft, "Symmetry breaking through bell-jackiw anomalies," *Phys. Rev. Lett.*, vol. 37, pp. 8–11, Jul 1976.

[6] G. 't Hooft, "Computation of the quantum effects due to a four-dimensional pseudoparticle," *Phys. Rev. D*, vol. 14, pp. 3432–3450, Dec 1976.

[7] C. A. Baker *et al.*, "An Improved experimental limit on the electric dipole moment of the neutron," *Phys. Rev. Lett.*, vol. 97, p. 131801, 2006.

[8] V. Baluni, "CP-nonconserving effects in quantum chromodynamics," *Phys. Rev. D*, vol. 19, pp. 2227–2230, Apr 1979.

[9] "Chiral estimate of the electric dipole moment of the neutron in quantum chromodynamics: R.j. crewther, p. di vecchia. g. veneziano and e. witten phys. lett. 88b (1979) 123.," *Physics Letters B*, vol. 91, no. 3–4, pp. 487 –, 1980.

[10] R. Crewther, P. D. Vecchia, G. Veneziano, and E. Witten, "Chiral estimate of the electric dipole moment of the neutron in quantum chromodynamics," *Physics Letters B*, vol. 88, no. 1–2, pp. 123 – 127, 1979.

[11] W. A. Bardeen, S.-H. Tye, and J. Vermaseren, "Phenomenology of the new light higgs boson search," *Physics Letters B*, vol. 76, no. 5, pp. 580 – 584, 1978.

[12] R. Peccei, T. T. Wu, and T. Yanagida, "A viable axion model," *Physics Letters B*, vol. 172, no. 3–4, pp. 435 – 440, 1986.

[13] J. E. Kim, "Weak-interaction singlet and strong CP invariance," *Phys. Rev. Lett.*, vol. 43, pp. 103 – 107, Jul 1979.

[14] M. Shifman, A. Vainshtein, and V. Zakharov, "Can confinement ensure natural {CP} invariance of strong interactions?," *Nuclear Physics B*, vol. 166, no. 3, pp. 493 – 506, 1980.

[15] M. Dine and W. Fischler, "The not-so-harmless axion," *Physics Letters B*, vol. 120, no. 1–3, pp. 137 – 141, 1983.

[16] G. G. Raffelt, *Stars as laboratories for fundamental physics : the astrophysics of neutrinos, axions, and other weakly interacting particles*. University of Chicago Press, 1996.

[17] M. S. Turner, "Windows on the axion," *Physics Reports*, vol. 197, no. 2, pp. 67 – 97, 1990.

[18] K. A. Olive *et al.*, "Review of Particle Physics," *Chin. Phys.*, vol. C38, p. 090001, 2014.

[19] M. Fukugita, S. Watamura, and M. Yoshimura, "Light pseudoscalar particle and stellar energy loss," *Phys. Rev. Lett.*, vol. 48, pp. 1522–1525, May 1982.

[20] J. Preskill, M. B. Wise, and F. Wilczek, "Cosmology of the invisible axion," *Physics Letters B*, vol. 120, no. 1–3, pp. 127 – 132, 1983.

[21] L. Abbott and P. Sikivie, "A cosmological bound on the invisible axion," *Physics Letters B*, vol. 120, no. 1–3, pp. 133 – 136, 1983.

[22] P. Fox, A. Pierce, and S. D. Thomas, "Probing a QCD string axion with precision cosmological measurements," 2004.

[23] D. N. Spergel *et al.*, "Wilkinson Microwave Anisotropy Probe (WMAP) three year results: implications for cosmology," *Astrophys. J. Suppl.*, vol. 170, p. 377, 2007.

[24] J. Jaeckel and A. Ringwald, "The Low-Energy Frontier of Particle Physics," *Ann. Rev. Nucl. Part. Sci.*, vol. 60, pp. 405–437, 2010.

[25] J. E. Moody and F. Wilczek, "New macroscopic forces?," *Phys. Rev. D*, vol. 30, pp. 130–138, Jul 1984.

[26] S. L. Cheng, C. Q. Geng, and W.-T. Ni, "Axion-photon couplings in invisible axion models," *Phys. Rev. D*, vol. 52, pp. 3132–3135, Sep 1995.

[27] M. Dine, W. Fischler, and M. Srednicki, "A simple solution to the strong {CP} problem with a harmless axion," *Physics Letters B*, vol. 104, no. 3, pp. 199 – 202, 1981.

[28] M. E. Sainio, *Chiral Dynamics: Theory and Experiment: Proceedings of the Workshop Held at MIT, Cambridge, MA, USA, 25–29 July 1994*, ch. Pion-nucleon sigma term, pp. 212–223. Berlin, Heidelberg: Springer Berlin Heidelberg, 1995.

[29] G. Raffelt, "Limits on a *cp*-violating scalar axion-nucleon interaction," *Phys. Rev. D*, vol. 86, p. 015001, Jul 2012.

[30] J. Leitner and S. Okubo, "Parity, charge conjugation, and time reversal in the gravitational interaction," *Phys. Rev.*, vol. 136, pp. B1542–B1546, Dec 1964.

[31] "Experimental tests for some quantum effects in gravitation," *Annals of Physics*, vol. 107, no. 1, pp. 337 – 359, 1977.

[32] Y. Fujii, "Scale invariance and gravity of hadrons," *Annals of Physics*, vol. 69, no. 2, pp. 494 – 521, 1972.

[33] E. Fischbach, D. Sudarsky, A. Szafer, C. Talmadge, and S. H. Aronson, "Fischbach *et al.* respond," *Phys. Rev. Lett.*, vol. 56, pp. 2424–2424, Jun 1986.

[34] R. C. Ritter, L. I. Winkler, and G. T. Gillies, "Search for anomalous spin-dependent forces with a polarized-mass torsion pendulum," *Phys. Rev. Lett.*, vol. 70, pp. 701–704, Feb 1993.

[35] P. Vorobyov and Y. Gitarts, "A new limit on the arion interaction constant," *Physics Letters B*, vol. 208, no. 1, pp. 146 – 148, 1988.

[36] S. A. Hoedl, F. Fleischer, E. G. Adelberger, and B. R. Heckel, "Improved constraints on an axion-mediated force," *Phys. Rev. Lett.*, vol. 106, p. 041801, Jan 2011.

[37] G. D. Hammond, C. C. Speake, C. Trenkel, and A. P. Patón, "New constraints on short-range forces coupling mass to intrinsic spin," *Phys. Rev. Lett.*, vol. 98, p. 081101, Feb 2007.

[38] A. N. Youdin, D. Krause, Jr., K. Jagannathan, L. R. Hunter, and S. K. Lamoreaux, "Limits on spin-mass couplings within the axion window," *Phys. Rev. Lett.*, vol. 77, pp. 2170–2173, Sep 1996.

[39] W.-T. Ni, S.-s. Pan, H.-C. Yeh, L.-S. Hou, and J. Wan, "Search for an axionlike spin coupling using a paramagnetic salt with a dc squid," *Phys. Rev. Lett.*, vol. 82, pp. 2439–2442, Mar 1999.

[40] B. Baiboussinov, C. Braggio, A. Cardini, G. Carugno, F. Congiu, S. Gain, G. Galeazzi, A. Lai, A. Lehman, P. Mocci, A. Mura, F. Quochi, M. Saba, B. Saitta, and G. Sartori, "An active electron polarized scintillating GSO target for neutrino physics," *Nuclear Instruments and Methods in Physics Research A*, vol. 694, pp. 335–340, Dec. 2012.

[41] J. Clarke and A. I. Braginski, eds., *The SQUID Handbook: Fundamentals and Technology of SQUIDs and SQUID Systems*. Wiley-VCH, 2005.

[42] N. Ashcroft and N. Mermin, *Solid State Physics*. Cengage Learning, 2011.

[43] L. Landau and E. Lifshitz, *Statistical Physics*. No. v. 5, Elsevier Science, 2013.

[44] W. Bialek, J. Moody, and F. Wilczek, "Macroscopic t nonconservation: Prospects for a new experiment," *Phys. Rev. Lett.*, vol. 56, pp. 1623–1626, Apr 1986.

[45] MAGNICON, *1-stage Current Sensor C6XXL1W Data Sheet*.

[46] W.-T. Ni, "A Scheme for a spin coupling experiment in space using magnetic materials with a DC SQUID," *Class. Quant. Grav.*, vol. 13, pp. A135–A141, 1996.

[47] B. J. Venema, P. K. Majumder, S. K. Lamoreaux, B. R. Heckel, and E. N. Fortson, "Search for a coupling of the earth's gravitational field to nuclear spins in atomic mercury," *Phys. Rev. Lett.*, vol. 68, pp. 135–138, Jan 1992.

[48] E. Fischbach and C. Talmadge, *The Search for Non-Newtonian Gravity*. AIP-Press S, Springer New York, 1998.

[49] D. J. Wineland, J. J. Bollinger, D. J. Heinzen, W. M. Itano, and M. G. Raizen, "Search for anomalous spin-dependent forces using stored-ion spectroscopy," *Phys. Rev. Lett.*, vol. 67, pp. 1735–1738, Sep 1991.

[50] J. Daniels and W.-T. Ni, "A torsion balance search for long-range spin-dependent forces using polarized nuclei," *Physica B: Condensed Matter*, vol. 194–196, Part 1, pp. 149 – 150, 1994.

[51] C.-H. Hsieh, P.-Y. Jen, K.-L. Ko, K.-Y. Li, W.-T. Ni, S.-S. Pan, Y.-H. Shih, and R.-J. Tyan, "The equivalence principle experiment for spin-polarized bodies," *Modern Physics Letters A*, vol. 4, no. 17, pp. 1597–1603, 1989.

[52] A. Arvanitaki and A. A. Geraci, "Resonantly detecting axion-mediated forces with nuclear magnetic resonance," *Phys. Rev. Lett.*, vol. 113, p. 161801, Oct 2014.

[53] P.-H. Chu, E. Weisman, C.-Y. Liu, and J. C. Long, "Search for exotic short-range interactions using paramagnetic insulators," *Phys. Rev. D*, vol. 91, p. 102006, May 2015.

[54] A. Papoulis and S. Pillai, *Probability, random variables, and stochastic processes*. McGraw-Hill electrical and electronic engineering series, McGraw-Hill, 2002.

[55] M. Matsumoto and T. Nishimura, "Mersenne twister: a 623-dimensionally equidistributed uniform pseudo-random number generator," *ACM Transactions on Modeling and Computer Simulation (TOMACS)*, vol. 8, no. 1, pp. 3–30, 1998.

[56] A. Vinante, R. Mezzena, G. A. Prodi, S. Vitale, M. Cerdonio, P. Falferi, and M. Bonaldi, "Dc superconducting quantum interference device amplifier for gravitational wave detectors with a true noise temperature of 16 μk," *Applied Physics Letters*, vol. 79, no. 16, pp. 2597–2599, 2001.

[57] A. Vinante, R. Mezzena, G. A. Prodi, S. Vitale, M. Cerdonio, P. Falferi, and M. Bonaldi, "Dc superconducting quantum interference device amplifier for gravitational wave detectors with a true noise temperature of 16 μk," *Applied Physics Letters*, vol. 79, no. 16, pp. 2597–2599, 2001.

[58] P. Falferi, M. Cerdonio, L. Franceschini, R. Macchietto, S. Vitale, and J. P. Zendri, "A high inductance khz resonator with a quality factor larger than 10^6," *Review of Scientific Instruments*, vol. 65, no. 9, pp. 2916–2919, 1994.

[59] L. Carbone, H. Panjwani, and C. C. Speake, "Design of high-density electron spin-polarized test masses," *Classical and Quantum Gravity*, vol. 26, no. 14, p. 145009, 2009.

[60] B. Franke, *Investigations of the Internal and External Magnetic Fields of the Neutron Electric Dipole Moment Experiment at the Paul Scherrer Institute*. PhD thesis, PSI, Villigen, 2013.

[61] L. Baggio, M. Bignotto, M. Bonaldi, M. Cerdonio, L. Conti, P. Falferi, N. Liguori, A. Marin, R. Mezzena, A. Ortolan, S. Poggi, G. A. Prodi, F. Salemi, G. Soranzo, L. Taffarello, G. Vedovato, A. Vinante, S. Vitale, and J. P. Zendri, "3-mode detection for widening the bandwidth of resonant gravitational wave detectors," *Phys. Rev. Lett.*, vol. 94, p. 241101, Jun 2005.

[62] P. Svrcek and E. Witten, "Axions in string theory," *Journal of High Energy Physics*, vol. 2006, no. 06, p. 051, 2006.

[63] T. Sleator, E. L. Hahn, C. Hilbert, and J. Clarke, "Nuclear-spin noise," *Phys. Rev. Lett.*, vol. 55, pp. 1742–1745, Oct 1985.

[64] I. P. Stern, "Axion Dark Matter Searches," *AIP Conf. Proc.*, vol. 1604, pp. 456–461, 2014.

[65] G. D. Hammond, A. Pulido Patón, C. C. Speake, C. Trenkel, G. K. Rochester, D. Shaul, and T. J. Sumner, "New spin source to search for scalar-pseudoscalar couplings at short range," *Phys. Rev. D*, vol. 77, p. 036005, Feb 2008.